Experiments on Internal Waves: Propagation and Reflection

by

©Prajvala Kishore Kurtakoti

A Thesis submitted to the School of Graduate Studies in partial fulfillment of the requirements for the degree of

Master of Science

Department of Physics and Physical Oceanography

Memorial University of Newfoundland

October 2014

St. John's Newfoundland

Abstract

Internal waves are present both in the atmosphere and the oceans. Internal waves transport momentum across long distances and their breaking provides energy for mixing. The mechanisms of internal wave dissipation and breaking is not completely understood. We are interested in understanding how internal waves propagate and reflect off sloping topography such as the continental shelf and dissipation. We conducted a series of laboratory experiments to study the energy flux of propagating and reflecting mode-1 vertically trapped internal waves in a linearly stratified salt water fluid. The internal waves are generated by a wave generator that is capable of producing monochromatic vertical mode-1 internal waves. In our experiments, we record a video in a rectangular section of the tank where these waves propagate along the length of the tank (5m) and reflect back. We repeated this for 3 different types of end wall boundary conditions : no slope, supercritical slope and subcritical slope. Their quantitative measurements of the structure and amplitude of the internal waves are measured using an optical technique called synthetic schlieren from which we can extract the energy flux of the wave. We use a complex demodulation function called the Hilbert transform to filter out internal waves on the basis of the sign of their wave vector. We employ this technique to filter out the generated waves that are travelling left to right from their reflection that are travelling right to left. From the filtered data we can understand how much energy from incoming waves is present in reflected

internal waves and how internal waves dissipate across experiments from all the cases and across different wave generator amplitudes. The analysis of energy flux of internal waves during propagation and reflection using Hilbert transform is helpful as it brings insight into phenomena that are difficult to observe during field studies. Comparison between the reflected energy efficiency across the 3 types of experiments improves our understanding of how waves reflect from different end boundaries, and also sheds light on the how dissipation changes when we change wave generator amplitude.

Acknowledgements

I would like to first and foremost acknowledge my supervisor Dr. James Munroe for his immense support and patience. His eagerness to share his knowledge with his students and motivate original research in the laboratory has truly inspired me as a researcher. For helping me bridge the gap between my Computer Science Bachelors and Physical Oceanography Masters through constant encouragement and teaching I am deeply indebted to him. Building a stratified fluids laboratory from scratch with this dedicated lab group has been an amazing learning experience for me. I would also like to thank my professors, Entcho Demirov and Iakov Afanassiev for introducing me to GFD and Numerical modeling. Their pedagogy has innately helped me in understanding my research. I would also like to thank my fellow Stratified Fluids lab mate Fan Lin for many experimental discussions and useful suggestions.

I would like to sincerely thank my parents Premalatha and Kishore Kurtakoti for supporting and encouraging me in moving to a foreign country to pursue my graduate studies. Their patience and love has helped me through more than I can write here. Their faith in my abilities has given me confidence on days when I didn't have any.

I want to deeply thank my best friend Pooja Subramaniam for visiting me here from India and supporting me when I was homesick. I would also like to thank my friends Tarun Verma, Gopi Kishore, Haripriyai Sekaran, Nonna Belalov and Siva Prasad for making my stay in St.John's so much closer to home.

Table of Contents

List of Tables

List of Figures

Chapter 1

Introduction

The study of internal gravity waves has gained a lot of importance in recent years due to a renewed understanding of its importance in atmospheric and oceanic systems. In this chapter, we give a brief introduction to internal gravity waves and the role they play in our atmosphere and ocean in transporting energy and momentum. We explain our motivation for studying internal waves through laboratory experiments. We then discuss the current literature in the study of internal gravity waves both in the open ocean and laboratory experiments.

We have commonly observed surface waves oscillating up and down when we go to a beach or a lake. Surface waves occur at the interface of air and water, and when the water surface is lifted from its equilibrium position due to a disturbance, it experiences a restoring force that makes it come back but if it overshoots the equilibrium position then again due to the restoring forced, it comes back up again thus oscillating about the equilibrium position. This spring-like motion is mainly due to buoyancy which is due to gravity and hence surface waves are sometimes called gravity waves. Now imagine a two layer fluid where the heavier fluid lies below the lighter fluid. If the interface between these two layers a disturbed, the interface will oscillate just like a

surface wave. These waves are called internal gravity waves. Internal gravity waves are waves that move within a fluid. For internal waves to exist the fluid medium must be stratified. In stratified fluids, the fluid's density changes with height. In the deep ocean, internal waves can have amplitudes as large as 300 m.

1.1 Motivation

Internal waves are mysterious and interesting due to several reasons. Internal waves are very difficult to observe. Unlike surface waves it is almost impossible to observe internal waves propagating in the interior of the ocean. Oceanic internal waves are sometimes spotted by the sea surface roughness. Atmospheric internal waves are sometimes visualized by formation of wave clouds. Studying internal waves experimentally are also hard for the same reason. Measuring and visualizing internal waves is quite a challenge. Mathematically internal waves are interesting because unlike surface waves, the phase velocity $\vec{C_p}$ and the group velocity $\vec{C_g}$ of internal waves propagate at right angles to each other. Internal waves propagate in such a way that they force the fluid to move along a line at an angle θ to the vertical and oscillate with the frequency of the internal wave. Internal waves cannot be generated if the frequency of generation is greater than the buoyancy frequency of the fluid medium. Internal waves are geophysically significant because they play an important role in the transfer of momentum and also provide mechanisms to help in mixing. We are interested in the generation mechanisms and in studying the evolution of propagating internal waves. Studying the evolution of propagating internal waves means we try to measure the transport of energy of generated internal waves as they move across the tank to see how much energy is lost in dissipation and what happens when they meet an obstacle. We study internal waves using laboratory experiments. Generating and

analyzing internal waves experimentally can be done with high confidence and help us build and validate theories on internal wave dynamics. In this thesis, we mainly study $mode-1$ internal waves (mode -1 internal waves are explained in detail in section 2.2.1), their generation mechanism, propagation, and reflection with different boundaries. This is a preliminary step towards understanding how internal waves reflect off sloping topography such as the continental shelf. We performed a series of laboratory experiments to study various parameters of propagating and reflecting mode-1 internal waves in a continuously stratified salt water fluid. We then used a technique called the Hilbert transform to separate out mode-1 waves traveling in different directions. This is useful as it allows us to measure energetics of the reflected waves and allows us to compare it to the energetics of the incoming waves. We also compare theoretical predictions of various parameters of the mode-1 internal waves and compare it to the experimentally measured values.

1.1.1 Internal gravity waves in ocean and atmosphere

Atmospheric internal waves occur when a stratified air blows over an obstacle (like a mountain). When this stratified layer hits the obstacle, horizontal layers of air of uniform density get disturbed and this disturbance can get launched into internal waves which can sometimes create wave clouds.

In the ocean, cold and dense salt water is formed in the polar regions and as they are heavier than the surrounding water they sink to the bottom of the ocean floor. For it to sink as a separate water mass, it must not mix with the surrounding water for a steady state to be achieved [10]. It has been speculated that internal waves are the cause of this mixing. Internal waves are also responsible for the transfer of momentum over large distances ($1000-3000$ km) in the ocean from the deep ocean onto the continental slope [9].

Another major example of internal waves in the oceans are the internal tides. Internal tides are internal gravity waves that are generated in the ocean when surface tides force ocean's stratified water over varying bottom topography. Christopher Garrett and Eric Kunze [2] noted that tidal internal waves generated by surface tides moving over gigantic mid-ocean ridges radiate away as large-scale internal waves. These internal waves break sometimes on continental slopes and play an important role in the mixing and transport of heat, salt, nutrients, and other suspended matter. This mixing introduces nutrients into the water column and fertilizes the local region making it biologically very productive [12]. Such sites are often the breeding grounds for commercially important fishes and the knowledge of such sites are very relevant for fishing industries. Thus while quantifying the role internal waves in energy, mass and momentum transport is a key research area in physical oceanography, their implications are very important to responsibly harnessing earth's resources.

In places with large structures in the ocean and large sea-level changes leads to generation of solitary internal tides which can be very large that they can be a safety and environmental concern for off-shore drilling operations [4]. Solitary waves are a class of non-linear, isolated waves of complex shape that occur frequently in the ocean. These waves can be more than 100 m tall and these large amplitude waves create strong currents that are proven to be a hazard for off-shore structures and drilling operations [11]. The influence of internal solitons in regions where they are observed should not be neglected while designing off-shore platforms.

1.1.2 Internal gravity waves in laboratory experiments

An advantage of studying internal waves experimentally is that we get to work on a simplified experimental set-up and build it in complexity with growing understanding. But like internal waves in atmosphere and oceans, internal waves generated in labo-

ratory experiments can also be very hard to visualize and measure. Another problem in studying internal waves in the laboratory is generation of internal waves. We shall now see how these problems have been tackled in the past.

Over the last two centuries great progress has been made in the field of visualizing internal waves starting with the Schlieren technique invented by the German physicist August Toepler [15] . One of the first laboratory experiments conducted to test the linear theory of internal waves in stratified fluids is the oscillating cylinder experiment by Mowbray and Rarity in 1967 [8]. They used a visualization technique which is a predecessor to a modern optical technique (traditional Schlieren method) that is one of the most effective and non-intrusive methods to visualize internal waves in stratified fluid. The traditional schlieren techniques are fundamentally based on Snell's law which describes the bending of light rays when it passes through a medium of varying density [16]. When light rays pass through a medium which has changing refractive indices, the path of light is deflected from its original track and it undergoes a phase change. Optical techniques (such as Shadowgraph, Interferometry, Schlieren methods) were used to detect this deflection. From the deflection, it was possible to extract changes in refractive indices and thus density changes in the fluid could be measured. We started our experimental study by repeating this experiment by visualizing the internal waves generated by a vertically oscillating cylinder. The visualization method of the internal waves generated in our laboratory is based on a digital variant of the Schlieren methods [1] called the 'synthetic schlieren′ and is explained in detail in Chapter 3. Using synthetic schlieren we are able to quantitatively measure the perturbation in the density field and from that we can measure the amplitude and energy flux of the internal waves.

We needed to design an internal wave generator for experimental applications. It is based on an existing internal wave generator designed by Gostiaux, Didelle, Mercier

and Dauxois in 2010 [6]. The wave generator is capable of producing sinusoidal vertically trapped mode-1 internal waves that travel along the length of the tank. Mode-1 internal waves are found in the ocean in the form of internal tides and are frequently observed. We study how these internal waves propagate and interact with different end boundary conditions.

1.2 Theory of internal waves in linearly stratified fluid

Let us now consider the dynamics of small-amplitude internal waves that are in a linearly stratified fluid. In our laboratory experiments, the internal waves are considered two-dimensional occurring in the $x-z$ plane, non-rotational, with no background flow.

1.2.1 Buoyancy frequency

Consider a fluid parcel in a stratified fluid where the density of the fluid increases linearly with depth. Now if we raise a fluid parcel from depth z of density ρ_0 to $z+h$ where the ambient density $\rho_0 - \delta_\rho$ is less than the density of the fluid parcel. If the fluid is incompressible then the fluid parcel will experience a net downward force equal to the difference of the weight of the fluid parcel and that of the displaced parcel. From Newton's second law,

$$\rho_0 V \frac{d^2\delta_z}{dt^2} = -\delta_\rho V g \tag{1.1}$$

Where V is the volume of the fluid parcel, g is acceleration due to gravity. Since the magnitude of density changes are very small,

$$\delta_\rho \simeq \frac{-d\bar{\rho}}{dz}\delta_z \tag{1.2}$$

where δ_ρ is the difference in density of the fluid parcels at z and $z+h$ respectively and δ_z is the displacement of the fluid parcel.

$$\rho_0 \frac{d^2\delta_z}{dt^2} = \frac{g d\bar{\rho}}{dz}\delta_z \tag{1.3}$$

$$\frac{d^2\delta_z}{dt^2} - \frac{g}{\rho_0}\frac{d\bar{\rho}}{dz}\delta_z = 0 \tag{1.4}$$

which can be rewritten as

$$\frac{d^2\delta_z}{dt^2} + N^2\delta_z = 0 \tag{1.5}$$

where,

$$N^2 = -\frac{g}{\rho_0}\frac{d\bar{\rho}}{dz} \tag{1.6}$$

The equation 1.5 has the same form as the equation of motion of a simple harmonic motion in which N refers to the frequency of oscillation. Equation 1.6 describes the buoyancy frequency of a Boussinesq fluid. It is sometimes called the "Brunt-Väisälä frequency". This means that a vertically displaced fluid parcel will oscillate at an angular frequency N, whose corresponding buoyancy period would be $2\pi/N$ s.

Now let us consider another case of a fluid parcel being displaced from its position by a small distance δ_l along a line at an angle θ to the vertical. We further assume that the consequent parcel motion is constrained to move along this line. Even though it may seem unrealistic, let us go with the thought for the moment. The new downward

force will be given by,

$$\rho_0 \frac{d^2\delta_l}{dt^2} = -\delta_\rho g \cos\theta \tag{1.7}$$

where $g\cos\theta$ is the component of downward gravitational force that is exerted along the line at angle θ. And following the same steps which helped us arrive at equation 1.5, we get,

$$\frac{d^2\delta_l}{dt^2} + \omega^2\delta_l = 0 \tag{1.8}$$

where

$$\omega = N\cos\theta \tag{1.9}$$

where $N\cos\theta$ is the frequency of oscillation of a fluid parcel that moves along a line at an angle θ. Surprisingly enough, if the oscillations are vertical then, $\theta = 0$ and $\omega = N$. This is the dispersion relation for internal waves in linearly stratified fluids.

1.2.2 Equations of motions of internal waves in a Boussinesq fluid

The equations governing geophysical flows are greatly simplified when we apply the Boussinesq approximation along with the assumption that the fluid is incompressible. These equations are discussed in basic fluid dynamics textbooks [13] and consist of the momentum conservation equations, the internal energy equation and the continuity equation.

$$\rho_0 \left(\frac{Du}{Dt} - f_0 v\right) = -\frac{\partial p}{\partial x} \tag{1.10}$$

$$\rho_0 \left(\frac{Dv}{Dt} - f_0 u\right) = -\frac{\partial p}{\partial y} \tag{1.11}$$

$$\rho_0 \left(\frac{Dw}{Dt}\right) = -\frac{\partial p}{\partial z} - g\rho \tag{1.12}$$

$$\frac{D\rho}{Dt} = -w\frac{d\bar{\rho}}{dz} \tag{1.13}$$

$$\bigtriangledown.\vec{u} = 0 \tag{1.14}$$

where (u, v, w) are components of the velocity vector $\vec{u}$, p is the dynamic pressure, $\bar{\rho}$ is the background density, ρ is the fluctuation density, ρ_0 is the characteristic density and D/Dt is called the material derivative,

$$\frac{D}{Dt} = \frac{\partial}{\partial t} + u\frac{\partial}{\partial x} + v\frac{\partial}{\partial y} + w\frac{\partial}{\partial z} \tag{1.15}$$

For internal waves in oceans and lakes as well as for internal waves that are generated in laboratory experiments, we can rewrite the equations governing geophysical flows for a non-rotating , two-dimensional reference frame in terms of velocity $\vec{u} \equiv (u, w)$, dynamic pressure p, and the fluctuation density ρ as follows [13],

$$\rho_0 \left(\frac{Du}{Dt}\right) = -\frac{\partial p}{\partial x} \tag{1.16}$$

$$\rho_0 \left(\frac{Dw}{Dt}\right) = -\frac{\partial p}{\partial z} - g\rho \tag{1.17}$$

$$\frac{D\rho}{Dt} = -w\frac{d\bar{\rho}}{dz} \tag{1.18}$$

$$\bigtriangledown.\vec{u} = 0 \tag{1.19}$$

and the background pressure, $\bar{p}$ is assumed to be in hydrostatic balance with the background density ρ as

$$\frac{d\bar{p}}{dz} = -g\bar{\rho} \tag{1.20}$$

If we are looking at small-amplitude internal waves in a fluid with no mean background flow we can ignore the advection terms in the material derivative. These non-linear terms are ignored as they are a function of the squared amplitude of the internal

waves which are small compared to the linear terms. We can replace D/Dt with $\partial/\partial t$ in equations 1.16 - 1.18. Now in order to reduce these four equations containing four unknowns to one equation with one unknown we take the curl of the momentum equations 1.16 - 1.17,

$$\frac{\partial}{\partial z}\left(\rho_0\left(\frac{Du}{Dt}\right)+\frac{\partial p}{\partial x}\right)-\frac{\partial}{\partial x}\left(\rho_0\left(\frac{Dw}{Dt}\right)+\frac{\partial p}{\partial z}+g\rho\right)=0 \tag{1.21}$$

$$\rho_0\frac{\partial \zeta}{\partial t}=g\frac{\partial \rho}{\partial x} \tag{1.22}$$

Where $\zeta=\partial_z u-\partial_x w$ is the relative vorticity.

Using streamfunction Ψ, we can describe $\vec{u}$ in terms of the gradient of the Ψ using the continuity equation 1.19

$$u=-\partial_z\Psi \tag{1.23}$$

$$w=\partial_x\Psi \tag{1.24}$$

and

$$\zeta=-(\partial_{xx}\Psi+\partial_{zz}\Psi)=-\bigtriangledown^2\,\Psi \tag{1.25}$$

Internal energy of a fluid parcel refers to its heat energy. The equation of internal energy used here ignores the thermodynamics of the deep ocean. The internal energy equation 1.13 can also be written in terms of the streamfunction as,

$$\frac{\partial^2\rho}{dt^2}=-\frac{\partial\Psi}{\partial x}\frac{d\bar{\rho}}{dz} \tag{1.26}$$

Eliminating ρ from 1.22 and 1.26 gives us the equation,

$$\frac{\partial^2}{\partial t^2}\bigtriangledown^2\,\Psi+N_0^2\frac{\partial^2}{\partial x^2}\Psi=0 \tag{1.27}$$

where N_0^2 is the squared buoyancy frequency whose definition is given in 1.6. In a linearly stratified fluid the buoyancy frequency term is a constant and hence represented as N_0.

1.2.3 Dispersion relation for internal waves

Two-dimensional waves can be represented by exponential solutions of the form,

$$\Psi = A_0 \exp[\imath(k_x x + k_z z - \omega t)] \tag{1.28}$$

where k_x, k_z are the horizontal and vertical wave numbers and ω is the angular frequency of the internal wave. Substituting this in the internal wave equation 1.27.

$$\omega^2 = N_0^2 \frac{k_x^2}{k_x^2 + k_z^2} \tag{1.29}$$

Equating the right hand side of the equation 1.29 to right hand side of the equation 1.9 we get,

$$\cos^2\theta = \frac{k_x^2}{k_x^2 + k_z^2} \tag{1.30}$$

If θ is the angle between sides k_x and k_z in a a right-angled triangle where $k_x^2 + k_z^2$ is the hypotenuse then another representation of the dispersion relation is,

$$\tan\theta = (k_z/k_x) \tag{1.31}$$

1.2.4 Polarization relations

For a linearly stratified fluid, the buoyancy frequency is a constant. Thus all the coefficients in the set of differential equations 1.16 - 1.19 are constants. In the previous section we saw how we can represent the various fields u, w, ρ, p in the form

given by the equation 1.28. We define z from 0 to Hcm where 0 is the surface of the water and H is the bottom of the tank. For real k_x, k_z and ω, we can write fields in the form 1.28 as

$$u = A_u e^{\iota(k_x x + k_z z - \omega t)} \tag{1.32}$$

$$w = A_w e^{\iota(k_x x + k_z z - \omega t)} \tag{1.33}$$

$$\rho = A_\rho e^{\iota(k_x x + k_z z - \omega t)} \tag{1.34}$$

$$p = A_p e^{\iota(k_x x + k_z z - \omega t)} \tag{1.35}$$

Substituting the above field in the equations 1.16 - 1.19 is equivalent to performing a Fourier transform. These equations are:

$$-\iota\omega A_u - \iota\frac{k_x}{\rho_0}A_p = 0 \tag{1.36}$$

$$-\iota\omega A_w + \iota\frac{k_z}{\rho_0}A_p + \frac{g}{\rho_0}A_p = 0 \tag{1.37}$$

$$-\iota\omega A_p - \frac{\rho_0 N_0^2}{g}A_w = 0 \tag{1.38}$$

$$\iota k_x A_u + \iota k_z A_w = 0 \tag{1.39}$$

We can see that the continuity equation gives us the relationship between the components of velocity.

$$A_u = -\frac{k_z}{k_x}A_w = -\tan\theta A_w \tag{1.40}$$

It means that the horizontal and vertical velocity components are either in phase or 180° out of phase. The ratio of horizontal to vertical velocity fields is $-\tan\theta$. Fluid parcels oscillate along a line that forms an angle θ with the vertical. This justifies the assumption we made while deriving the dispersion relation 1.9 for internal waves.

With internal waves, the vertical displacement field ξ is a useful measure of internal wave amplitude. However, in our laboratory experiments, we use synthetic schlieren to estimate the apparent displacement field from which we are able to construct the horizontal displacement field ς. In theory, for small amplitude internal waves, it is defined using the relation,

$$u = \frac{d\varsigma}{dt} \tag{1.41}$$

For mode-1 internal waves, the vertical displacement field and the horizontal displacement fields are 90° out of phase and are defined as,

$$\xi = A_\xi \cos(k_z z) \cos(k_x x - \omega t) \tag{1.42}$$

$$\varsigma = A_\varsigma \cos(k_z z) \sin(k_x x - \omega t) \tag{1.43}$$

Using the equation 1.41, we can get the horizontal velocity field in terms of the horizontal displacement field,

$$u = -\omega A_\varsigma \cos(k_z z) \cos(k_x x - \omega t) \tag{1.44}$$

Using the continuity equation 1.19,

$$\frac{\partial u}{\partial x} = -\frac{\partial w}{\partial z} \tag{1.45}$$

Solving for the vertical velocity field w using the equation 1.44 above, we get

$$w = -\omega \frac{k_x}{k_z} A_\varsigma \sin(k_z z) \sin(k_x x - \omega t) \tag{1.46}$$

We can relate ς to the dynamic pressure field using the horizontal momentum conser-

vation equation 1.16. Substituting,

$$\frac{\partial p}{\partial x} = \rho_0 \omega^2 A_\varsigma \cos(k_z z) \sin(k_x x - \omega t) \tag{1.47}$$

which upon integrating with respect to x gives the dynamic pressure field in terms of ς,

$$p = -\rho_0 \frac{\omega^2}{k_x} A_\varsigma \cos(k_z z) \cos(k_x x - \omega t) \tag{1.48}$$

We would also like to obtain the vertical displacement field in terms of the horizontal displacement field. For small amplitude waves w is related to ξ through the relation,

$$w = \frac{\partial \xi}{\partial t} \tag{1.49}$$

substituting for w from the equation 1.46 in the above equation and integrating with respect to time we get,

$$\xi = -\frac{k_x}{k_z} A_\varsigma \sin(k_z z) \cos(k_x x - \omega t) \tag{1.50}$$

Now we can easily get the fluctuation density field in terms of ς by substituting the vertical velocity field in terms of ς in the internal energy equation for internal waves 1.18 and integrating with respect to t,

$$\frac{\partial \rho}{\partial t} = -w \frac{d\bar{\rho}}{dz} = \frac{w N_0^2 \rho}{g} \tag{1.51}$$

$$\rho = -\frac{N_0^2 \rho_0}{g} \frac{k_x}{k_z} A_\varsigma \sin(k_z z) \cos(k_x x - \omega t) \tag{1.52}$$

In our laboratory experiments we use synthetic schlieren which gives us a measure of the apparent displacement field $\triangle z$ from which we are able to obtain the perturbation

to the squared buoyancy frequency $\triangle N^2$ [14]. In theory $\triangle N^2$ is given by the relation,

$$\triangle N^2 = -\frac{g}{\rho_0}\frac{\partial \rho}{\partial z} \tag{1.53}$$

Substituting ρ in terms of ς from the equation 1.52, we get the perturbation to the squared buoyancy frequency in terms of the horizontal displacement field,

$$\triangle N^2 = N_0^2 k_x A_\varsigma \cos(k_z z)\cos(k_x x - \omega t) \tag{1.54}$$

In addition, we may also compute the finite difference approximation to the time derivative of the squared buoyancy frequency, N_t^2 by calculating the apparent displacement field, $\triangle z$ at consecutive time intervals that are much smaller than the period of the internal waves. In theory N_t^2 is given by the relation,

$$N_t^2 = \frac{\partial \triangle N^2}{\partial t} = N_0^2 \omega k_x A_\varsigma \cos(k_z z)\sin(k_x x - \omega t) \tag{1.55}$$

From the definition of the horizontal displacement field 1.42, we can rewrite the above expression as,

$$N_t^2 = A_{N_t^2}\cos(k_z z)\sin(k_x x - \omega t) \tag{1.56}$$

where $A_{N_t^2} = k_x \omega N^2 A_\varsigma$ or we can write it in terms of ς as,

$$N_t^2 = \omega N_0^2 k_x \varsigma \tag{1.57}$$

The field N_t^2 is what we quantitatively measure using synthetic schlieren. Now we shall define certain cross-correlations to understand the transport properties of mode-1 internal waves. We define the horizontal energy flux as the cross-correlation of the product of the horizontal velocity term and the dynamic pressure term and the

vertical energy flux as the cross-correlation of the product of the vertical velocity term and the dynamic pressure term, and for both its considered over a time period of the mode-1 internal wave. The relations are given by,

$$\langle F_{E_x} \rangle = \langle pu \rangle \tag{1.58}$$

$$\langle F_{E_z} \rangle = \langle pw \rangle \tag{1.59}$$

Where $\langle\rangle$ represents cross-correlation. Expanding the right hand side by expressing them in terms of the horizontal displacement field ς we get vertical energy flux averaged over a time period,

$$\langle F_{E_z} \rangle = \frac{\rho_0 \omega^3 k_x}{k_z} A_\varsigma \cos(k_x x - \omega t) \sin(k_x x - \omega t) \langle \cos(k_z z) \sin(k_z z) \rangle = 0 \tag{1.60}$$

which is obvious as the internal waves generated are mode-1 vertically trapped internal waves. We expand the horizontal energy flux averaged over a time period as,

$$\langle F_{E_x} \rangle = \frac{\rho_0 \omega^3}{k_x} A_\varsigma^2 \cos^2(k_z z) \langle \cos^2(k_x x - \omega t) \rangle = \frac{1}{2} \frac{\rho_0 \omega^3}{k_x} A_\varsigma^2 \cos^2(k_z z) \tag{1.61}$$

We can introduce the horizontal energy flux in terms of the $\langle (N_t^2)^2 \rangle$ which is defined in 1.62 into the horizontal energy flux definition 1.61.

$$\langle (N_t^2)^2 \rangle = \frac{1}{2} k_x^2 \omega^2 N^4 A_\varsigma^2 \cos^2(k_z z) \tag{1.62}$$

We exclude k_x and simplify till we get the hozizontal energy flux in terms of the squared time derivative of the squared buoyancy frequency as,

$$\langle F_{E_x} \rangle = \frac{\rho_0}{N^3 k_z^3} \frac{\sqrt{(1 - (\frac{\omega}{N})^2}}{(\frac{\omega}{N})^2} \langle (N_t^2)^2 \rangle \tag{1.63}$$

We can also compute the vertically averaged horizontal energy flux $\langle\overline{F_{E_x}}\rangle$ as,

$$\langle\overline{F_{E_x}}\rangle = \frac{\rho_0}{N^3 k_z^3}\frac{\sqrt{(1-(\frac{\omega}{N})^2}}{(\frac{\omega}{N})^2}\langle\overline{(N_t^2)^2}\rangle \tag{1.64}$$

1.3 Internal waves near slopes

Internal wave interaction with slopes is very important to study in order to understand the role that internal waves play in transporting mass and momentum and their role in mixing. It is an important part of understanding ocean circulation and is of consequence for several industries. Internal waves have a unique property that is waves of a fixed frequency can propagate at a fixed angle to the vertical and this is independent of their wavelength and independent of the slope of the reflecting boundary [13]. In our laboratory, we have conducted experiments where the internal waves are incident upon a slope. The slope makes an angle α with the horizontal. If the angle of the internal wave is θ with the vertical then we can use the ratio, $\alpha/(\frac{\pi}{2}-|\theta|)$ to categorize if the slope is supercritical, subcritical and critical. In our experiments the slope was either supercritical, $\alpha/(\frac{\pi}{2}-|\theta|) > 1$ or subcritical, $\alpha/(\frac{\pi}{2}-|\theta|) < 1$.
To understand how reflection will occur at a supercritical or subcritical slope we now look at the figure 1.1. When internal waves are incident upon a subcritical slope, the waves reflect alternatively between the sloping boundary and the horizontal bottom surface and thus focusing the waves to the corner where the slope meets the bottom surface where the internal waves eventually dissipate. When internal waves are incident upon a supercritical slope, the waves reflect away from the point attractor and propagate away.

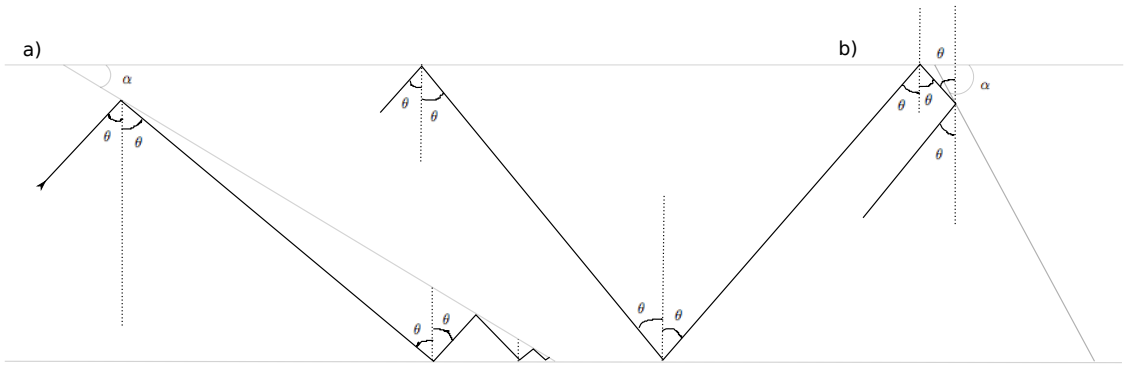

Figure 1.1: a) propagation of an internal wave ray incident upon a subcritical slope reflects in towards a point attractor and b) propagation of an internal wave ray incident upon a supercritical slope reflects away from the point attractor.

Chapter 2

Laboratory experiments and experimental analysis

2.1 Experiments

This chapter contains a description of the different laboratory experiments that were conducted on internal wave generation and propagation.

2.1.1 Internal waves generated using a vertically oscillating cylinder

The experiment for generating internal waves using a vertically oscillating cylinder is set-up as described. The experiments were performed separately in 2 transparent acrylic tanks one measuring 50 cm long, 20cm wide and 50 cm tall and the other measuring 488 cm long, 46cm wide and 52 cm tall . The tank is filled with linearly stratified salt water such that the density of water increases linearly with depth. The desired background linear stratification is achieved using the double bucket technique which is explained in great detail in section 2.2.10. A camera is placed a certain

distance away from the tank so as to minimize parallax error. A cylinder is placed in the interior of the fluid and is aligned such that the cross section of the cylinder faces the camera. The cylinder is held in place by a motorized bislide which is capable of oscillating the cylinder up and down a precise given distance which controls the amplitude of the internal waves generated and at a given frequency ω. The internal waves generated appear to be cross-shaped patterns and they obey the dispersion relation given by 1.6 and 1.29 and are valid for $\omega < N$. The internal wave pattern is schematically illustrated in figure . If the frequency of the oscillating cylinder is greater than w then we don't see any internal waves generated. They set up for the oscillating cylinder experiment is shown in figure .

We fix the amplitude of oscillation and record the internal waves generated for several times changing only the frequency of oscillation for every new experiment recorded and keeping every other variable constant. We use synthetic schlieren technique to visualize and get precise quantitative measurements of the internal waves generated in the tank.

2.1.2 Internal waves generated using a mode-1 internal wave generator

These experiments are performed in a transparent acrylic tank measuring 488 cm long, 46 cm wide and 52 cm tall. The tank is filled with linearly stratified salt water such that the density of water increases linearly with depth. The desired background linear stratification is achieved using the double bucket technique. A camera is placed a certain distance away from the tank so as to minimize parallax error. On one end of the tank we fix a wave generator that is capable of generating monochromatic mode-1 internal waves. The frequency of internal waves generated is controlled by the frequency of camshaft rotation which goes through the wave generator which is

controlled by a brushless DC motor attached at the top the camshaft. We set the frequency of the motor using a programmed controller and generate monochromatic internal waves that travel the length of the tank. Three types of experiments are possible based on the set-up on the other end of the tank, a simulated sloping topography whose slope can be supercritical or subcritical or just a vertical flat wall. We use synthetic schlieren techinque to visualize and get precise quantitative measurements of the internal waves generated in the tank. The set up for the mode-1 internal waves generated using a novel internal wave generator is given in the figure .

The frequency of the wavegenerator is fixed and we record the internal waves generated. The frequency of internal waves generated can be changed but for the 3 types of experimental set-up we have, we record internal waves generated at the same frequency.

2.2 Experimental tools

Experiments conducted on internal waves were performed using several lab equipments and experimental and analytical techniques. We also used a variety of equipments to prepare the set-up prior to performing the experiments. In this section we describe the experimental and analytical tools and their function.

2.2.1 Internal wave generator

Internal waves are often considered as monochromatic plane waves. But in laboratory conditions generating monochromatic waves has been very challenging. For the purposes of our laboratory experiments we require a wave generator that is capable of generating monochromatic mode-1 internal waves. L. Gostiaux, H. Didelle, S. Mercier and T. Dauxois [3] built a new internal wave generator that did this. We built an

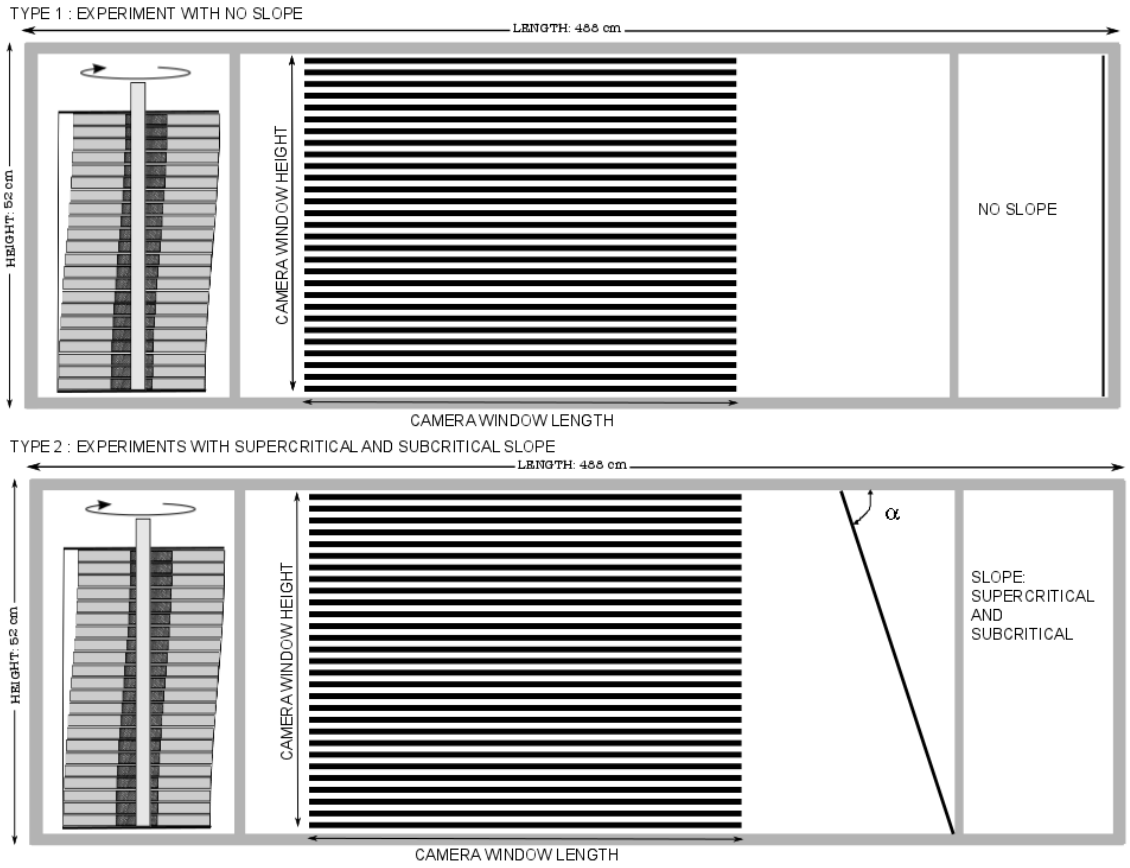

Figure 2.1: fig a) Experimental set-up (above) for studying internal wave propagation and reflection with a flat vertical end boundary condition and b) Experimental set-up (below) for studying internal wave propagation and reflection with a sloping end boundary condition. Based on the angle α, the slope of the end wall can be classified as sub-critical or super-critical. Experiments are conducted to study all three types of end wall conditions.

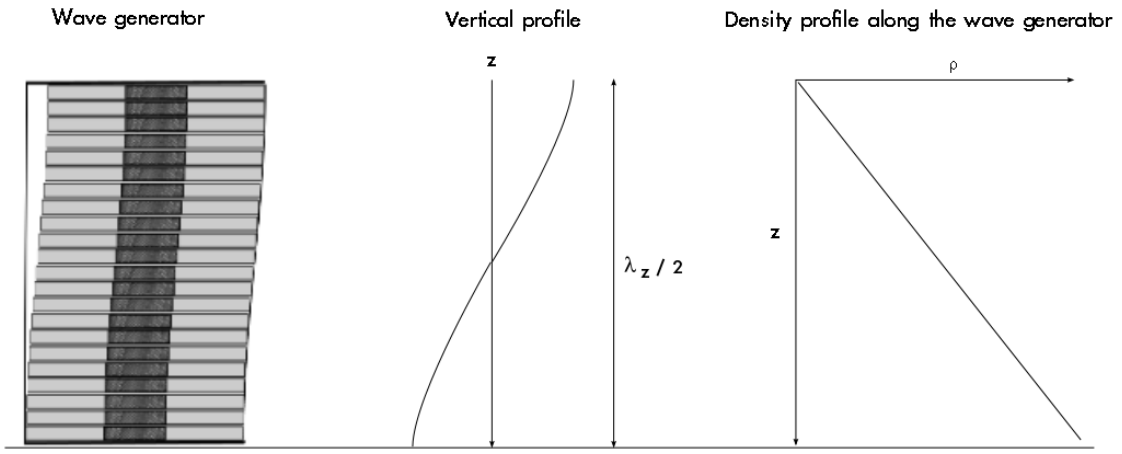

Figure 2.2: A side profile of the wave generator for generating monochromatic mode-1 internal waves. A phase-shifted cam shaft inside the wave generator allows the plates to move in a fashion that stays sinusoidally mode-1 in the vertical. The density profile from the top plate to the bottom plate of the wave generator increases linearly.

internal wave generator in our laboratory that was based on the wave generator [3] which has been designed for three purposes. Firstly, the oscillating boundary conditions force the fluid particles to propagate in one direction, hence reducing the mixing due to forcing. Second, only one ray tube is produced so that all of the energy is in the beam of interest. Third, temporal and spatial monochromaticity of the emitted beam is very high for the emitted beam. The strength of this technique is therefore the ability to produce monochromatic mode-1 internal waves. We modified their design of the wave generators so that it generated monochromatic $mode-1$ vertically trapped internal waves.

1. Description of the Wave generator:

   The generator consists of a pile of 26 1"thick PVC rectangular sheets arranged one over the other and enclosed in a transparent open box, free to slip over one another. The material chosen has the advantage that it is denser than the densest salt water we use to fill the tank and hence the wave generator automatically stays at the bottom of the tank. Since the plates are only slightly denser than the stratified fluid there is less friction between the plates. A rectangular hole in each plate allows a camshaft to go through the pile, imposing the relative position of the plates. The breadth of rectangular hole is such that the camshaft fits perfectly within it, i.e, the camshaft is as wide as the breadth of the rectangular hole. The plates are sinusoidally shifted due to helicoidal repartition of the cams. The rotation of the camshaft applies a periodic motion to the plates which propagates for a clockwise rotation. The amplitude of oscillation is 8cm peak to peak. The eccentricity of the camshaft defines the amplitude of oscillation of the plates. The vertical profile of the wave generator is shown in figure 2.2 and is a half cosine wave. The vertical profile and the height of the wave generator set the vertical wavelength, λ_z of the internal waves generated. Since the profile of the wave generator consist of only one half of the cosine wave, the vertical wavelength of the internal waves generated is twice the height of wave generator.

2.2.2 DMA 35 portable density meter

The DMA 35 protable density meter measures the density of liquids in g/cm^3 or kg/m^3 according to the oscillating U-tube principle. Apart from density you can select various further measuring units (relative density, density at reference temperature, concentrations). A temperature sensor measures the sample temperature right at the

measuring cell and displays it.

2.2.3 Micro-scale conductivity-temperature instrument

The micro-scale conductivity-temperature instrument (MSCTI) is designed to measure the temperature and electrical conductivity of water solutions containing conductive ions. The MSCTI provides two analog voltage outputs, one linearly proportional to the solution conductivity, and one non-linearly proportional to the solution temperature. The instrument is intended for use in moving solutions where spatial resolution and time response are important. The purpose of the MSCTI is to measure the conductivity of the stratified fluid in the transparent acrylic tank. These measurements are necessary for measuring the salinity which in turn are used in calculating the buoyancy frequency of the stratified fluid. Before using MSCTI for taking any measurements we must calibrate it.

Calibrating the MSCTI: First we make four saltwater solutions of different densities. Once they are at more or less the same temperature we measure their densities using a DMA 35 Portable Density Meter. The lowest and highest densities of the prepared salt solutions should match the lowest and highest densities of the stratified water in the transparent acrylic tank. Now the conductivity of the salt water solutions are measured by using a Mastercraft Deluxe Digital Volt Meter connected to the output of the MSCTI. The output is in the range of +/-5V. While measuring the conductivity of lowest salt solution we adjust the gain in MSCTI till the Voltmeter reads -5V. Once adjusted we measure conductivity of the remaining solutions. Knowing density and conductivity of the four solutions we use a least squares fit to fit a polynomial. This enables us to measure stratification of the tank using conductivity probe.

2.2.4 Masterflex 7592-82 benchtop controller with 7592-40 pump drive

The Modular Drive controls the speed of Masterflex I/P (Industrial/Process) pumps to provide flow rates from 0.12 to 13 L/min. We use Masterflex precision tubing with the pumps to ensure optimum performance. The pumps can be manually calibrated. We use it for filling up the transparent acrylic tank using the double bucket setup and for emptying the tank for cleaning etc.

2.2.5 Velmex motorized bislide and VXM stepping motor controller

The Velmex BiSlide is a modular system of positioning stages and hardware that allows you to quickly and easily create a complete single or multi-axis system by simply bolting together modular components. These components can be configured and assembled to form a work cell dedicated to a specific task. It is controlled and configured using a Stepping Motor Controller which is a complete controller with AC power supply package. It uses RS232 (serial port) communications for (Computer, PLC, PDA) programming. The Bislide controlled by the Stepping Motor Controller helps to traverse vertically at adjustable small speeds, any light weighted equipment attached to the bislide. In our experiment, we attach the Conductivity Probe to the Bislide and measure the conductivity of the stratified fluid of the transparent acrylic tank at all depths. From conductivity we can deduce salinity of the stratified fluid to measure the buoyancy frequency of the stratified fluid.

2.2.6 Manta G-125B camera with KOWA megapixel lens

The Manta G-125B is a low cost GigE Vision camera with a Sony ICX445 sensor. It runs at 6-7 frames per second,fps (full resolution- 30fps). Its a black and white camera. It is connected to a Kowa Megapixel lens with 25mm focal length. The camera is operated through a computer to start and stop capturing images. The captured images are transferred and stored in the computer via an ethernet cable.

2.2.7 LabJack U3-HV - USB multifunction data acquisition unit

It is a USB multifunction data acquisition and control device. It allows multiple devices to be connected to a PC and also allows us to stream and record data to the PC for data logging purposes. It has +/-10 Volt range on 4 input channels. For our experiments we connect the motorized Bislide, MSCTI, camera to the PC and operate it using Labjack.

2.2.8 Transparent acrylic tank

The experiments are conducted in a transparent, 1"thick acrylic tank. It has an aluminum base and sides for reinforcements. The dimensions of the tank are 488 cm long, 52 cm deep and 46 cm wide. The tank needs to be transparent for visualization and measurement of the internal waves.

2.2.9 Tote mixer

The Tote cap mounted tote mixer is used while executing the Double Bucket Technique. Its purpose is to keep the density of the salt water tank uniform everywhere inside it.

2.2.10 The double bucket technique

The traditional double bucket method consists of two buckets each filled with water of equal volume. The two buckets sit at equal height joined by a u-shaped tube running beneath the two tanks connecting them. There is also a hose joint to one of the buckets with a pump system attached. This pump is able to draw water from the bottom of this bucket. This bucket is referred to as the salt water bucket; the other bucket is referred to as the fresh water bucket. To obtain stratified fluid the two buckets are filled with fresh water to the appropriate height. Stoppers are placed in the various hose/tubes to avoid mixing. In the salt water bucket, salt is added to achieve a desired density of the experiment parameter. For every gram of salt that was added to the salt water bucket, one gram of fresh water is added to the fresh water bucket. This is done to avoid salt water rushing into the fresh water bucket when the stoppers are removed. The salt is mixed in thoroughly and once the double bucket system is in place near the tank, the stoppers are removed. A mixer in the salt water bucket keeps the water in the saltwater of a constant density. With the tank in place and stoppers removed, the pump is set in motion. The pump draws water from the salt water bucket, through the hose and into the tank. The hose lies on a sponge float like apparatus. The purpose of this is twofold; one, the hose always lies on the top of the surface of the water in the tank and two, the flowing water passes through the sponge in an effort to minimize disturbances of the stratified fluid.

The mechanics of the double bucket system are as follows. As the pump draws salt water from the bottom of the salt water bucket and out the hose, fresh water from the fresh water bucket will flow through the U-tube and into the salt water bucket. This reduces the relative salt concentration of the salt water and in turn it's density. In fact, for every infinitesimally small volume of salt water which is removed from the salt water bucket, half that amount in weight will be replaced with fresh water

by the fresh water bucket. As this process continues the double bucket system will fill the tank with the hose gently pouring water onto the surface of the water. The water leaving the hose progressively grows less and less dense until the both buckets are nearly empty and the density is approaching that of fresh water. When properly executed, this procedure will create a perfectly linear density profile.

We implement the double bucket technique in our lab using two 1100L capacity tanks and an industrial mixer to keep the salt water tank constantly mixed. The large tanks are necessary since the capacity of the transparent acrylic tank is 1167L and we need to add 20-40kg of salt into the salt water tank depending on the buoyancy frequency needed to be achieved for the experiment. A pipe connects the salt water tank to the fresh water tank and another pipe connects the salt water tank and the transparent acrylic tank in which we perform our experiments. We use two adjustable motor pumps to control the flow rate of water entering the salt water tank from the fresh water tank and of water leaving the salt water tank into the transparent acrylic tank. For achieving linear stratification the flow rate of the pipe connecting the salt water tank and the fresh water tank should be half the flow rate of the pipe connecting the salt water tank and the transparent acrylic tank.

2.3 Experimental analysis

2.3.1 Analytical tools

In this section we give a description of the software tools we use for Image processing, and the technique to measure and visualize internal waves.

2.3.1.1 Synthetic schlieren technique

For visualizing the internal waves we use an optical technique called the Synthetic Schlieren [14]. It is a noninvasive optical image processing technique for measuring the density perturbabtions in flows that can be assumed to be almost two-dimensional. We ignore the width-wise variations of the generated internal waves. The technique uses digital image processing to obtain precise measurements of the density gradient whose input is a sequence of images ('.png' format). Synthetic schlieren is motivated by the classical schlieren technique which has been used to visualize internal waves [7]. We have implemented the technique as published by [14] in Python programming language (Version 2.7.2) with a novel algorithm.

1. Theoretical determination of the internal wave deflection :

   When internal gravity waves evolve in a stratified fluid, isopycnal surfaces in the fluid are disturbed resulting in surfaces where the local density gradient either increases or decreases relative to the background density gradient. Background density gradient is the depthwise variation in density present when the fluid is completely at rest which we measure before beginning the experiment. When there are internal waves present in the view of the recording camera, the path of a nearly horizontal ray of light through stratified fluid is deflected due to changes in the refractive index gradient. This is due to the fact that there is a direct relationship between density ρ' fluctuations and refractive index n' fluctuations within the fluid, and by measuring the deflection of light rays passing through the solution we can measure the fluctuations in density gradient. This helps us measure the vertical displacement amplitude of the internal waves.

   The schematic used to synthetic schlieren in our laboratory is shown below in figure 2.3. Light rays radiate from an image back-illuminated in a TV and

enter a tank. The tank is divided lengthwise into 2 partitions and both are filled with the same salt stratified water. The partition that is close to the TV is always stationary and has no internal waves. The other partition is our test section where the internal waves originate and propagate. The partition is made of thin transparent PVC. The light rays that approach the camera from the TV are assumed to be nearly horizontal and their path is as follows: light rays pass through the first section of the tank which is stratified but has no internal waves and then pass through the second section of the tank where internal waves are expected to cause a deflection in the isopycnal surfaces of the fluid. Deflected rays then enter a camera, and the resulting data is transferred instantly and recorded into the computer through an ethernet cable. The raw data are a sequence of black and white images. The raw data is then processed using a software package that was developed by us for image processing in Python language. In our experiments, the back-illuminated image is a grid of horizontal black and white lines. The individual width of the black and white lines is known and recorded. The camera is placed as far as practical (typically 300 cm), so as to minimize the angle with which the light ray enters.

We use the method proposed by [14] to predict the internal wave field as follows. Consider the path followed by a light ray incident with an upward inclination upon a spanwise cross section of a tank filled with salt stratified water as shown in figure 2.3 . The curvature of ray through the tank in figure 2.3 is exaggerated for clarity. Because the index of refraction increases with salinity, the ray is refracted so that the angle of the ray above the horizontal decreases. Path taken by a ray of light satisfies the Snell's law,

$$n \cos \phi = constant \tag{2.1}$$

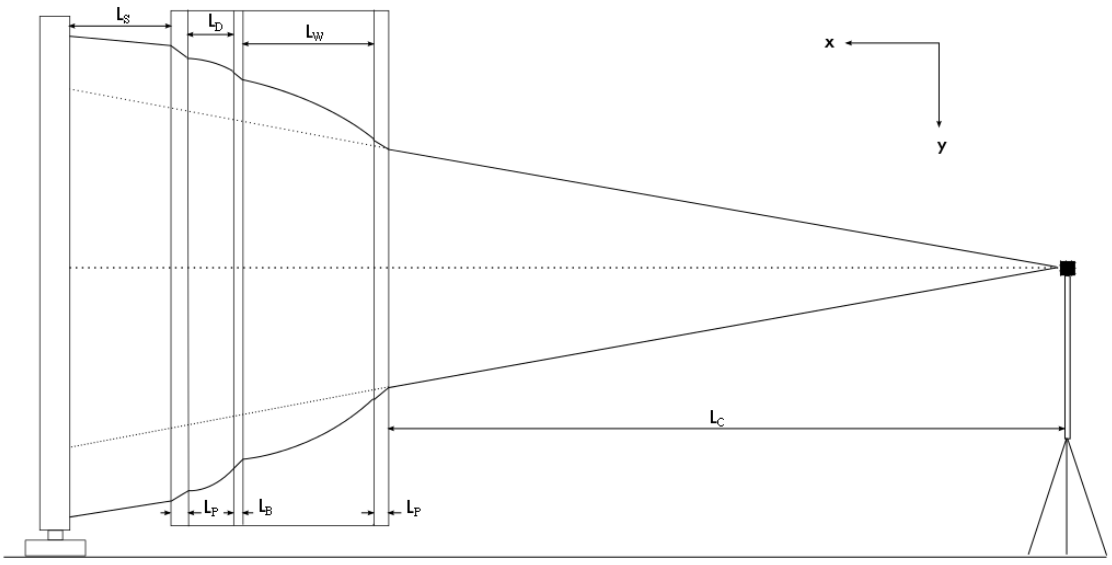

Figure 2.3: Schematic for showing the set-up for synthetic schlieren. The small dashed lines from the camera to the light source represent light rays which pass a tank of salt stratified water. The solid lines represents the deflected ray path taken if the density gradient (squared buoyancy frequency) changes due to the internal gravity waves. L_S, L_D and L_W are the distances between the TV screen and the back of the tank, the back of the tank and the barrier, the barrier and the front of the tank. L_P and L_B are the thicknesses of the wall of the tank and the barrier in the middle of the tank

in which n is the index of refraction of the medium and ϕ is the angle the light ray makes with surfaces of constant n, where z is the height, x is the distance along the tank, and y is the spanwise distance along the tank. We introduce along ray coordinate s and decompose this into co-ordinates $s_{\parallel}$ and $s_{\perp}$ to constant n. Differentiating 2.1 with respect to s, and noting that $ds_{\parallel}/ds = \cos\phi$ and $ds_{\perp}/ds = \sin\phi$, we obtain,

$$\frac{\partial n}{\partial s_{\perp}} \cos\phi \sin\phi - n \sin\phi \frac{d\phi}{ds} = 0 \tag{2.2}$$

Eliminating $d\phi/ds$ using $d^2 s_{\perp}/ds_{\parallel}^2 = \sec^3\phi d\phi/ds$ gives,

$$\frac{d^2 s_{\perp}}{ds_{\parallel}^2} = \frac{\sec^2\phi}{n} \frac{\partial n}{\partial s_{\perp}} \tag{2.3}$$

Ignoring variations along the ray in both ϕ and n provided $\partial n/\partial s_{\perp}$ remains finite and mod $ds_{\perp}/ds_{\parallel} << 1$, and integrating 2.3 using their values at the point of entry of the light ray into the tank. For two dimensional flows considered in our experiments, spanwise variations are ignored $n = n(x, z)$ and $s_{\parallel}$ coincides with the cross tank coordinate y. Furthermore, the condition mod $ds_{\perp}/ds_{\parallel} << 1$ linearizes 2.3 , thus allowing us to identify $s_{\perp}$ with either z to form 2 independent equations [14]:

$$\frac{d^2 z}{dy^2} = \frac{\sec^2\phi_i z}{n_i} \frac{\partial n}{\partial z} \tag{2.4}$$

where $\phi_i z$ is the angle that the incident light ray makes to the y axis in the vertical direction, and n_i is the index of refraction where the light ray is incident. We only consider vertical deflection of the light ray as described by 2.4. The experimental arrangement is such that mod $\phi < 5$ř and $\sec^2\phi_i z$ maybe taken

as unity. Except where strong mixing or layering occurs, it is valid to assume that the refractive index varies linearly over the small depth traversed by the light ray (typically less than 1cm) allowing us to replace the vertical gradient in n with the squared buoyancy frequency N^2 at the same level using the relationship,

$$\frac{\partial n}{\partial z} = \frac{dn}{d\rho}\frac{\partial \rho}{\partial z} = -\left(\frac{1}{g}\frac{\rho_0}{n_0}\frac{dn}{dp}\right) n_0 N^2 \tag{2.5}$$

Here ρ_0 and n_0 are reference values of the density and index of refraction, respectively. Because $dn/d\rho$ is approximately constant for salt water solutions (Weast, 1981), we write,

$$\frac{\partial n}{\partial z} = -n_0 \gamma N^2 \tag{2.6}$$

where

$$\gamma = \frac{1}{g}\frac{\rho_0}{n_0}\frac{dn}{dp} \approx 1.878 \times 10^{-4} s^2/cm \tag{2.7}$$

Subsituting 2.6 in 2.4 gives,

$$z\,(y) = z_i + y \tan\phi_i z - \frac{1}{2}\gamma N^2 y^2 \tag{2.8}$$

where z_i is the vertical position of the incident light ray. Repeated application of the Snell's Law together with 2.8 gives the total vertical deflection of a light ray travelling from the image screen to the camera as,

$$
\begin{aligned}
z\left(N^2,\phi_0\right) &= L_c\phi_0 \\
&+ L_p\left(\frac{n_a}{n_p}\right)\phi_0 \\
&+ L_w\left(\frac{n_a}{n_w}\right)\phi_0 - \frac{1}{2}\gamma N^2 L_w^2 \\
&+ L_b\left(\frac{n_a}{n_b}\phi_0 - \frac{n_w}{n_b}\gamma N^2 L_w\right) \\
&+ L_d\left(\frac{n_a}{n_w}\phi_0 - \gamma N^2 L_w\right) - \frac{1}{2}\gamma N^2 L_d^2 \\
&+ L_p\left(\frac{n_a}{n_p}\rho_0 - \frac{n_w}{n_p}\gamma N^2 L_w\right) - \gamma N^{@} L_d L_p \\
&+ L_s\left(\phi_0 - \frac{n_w}{n_a}\gamma N^2 L_w\right) - \gamma N^2 L_d L_s
\end{aligned}
\tag{2.9}
$$

If the isopycnal surfaces are locally perturbed by the internal gravity waves, then N^2 is changed and a light ray passing through the wave field is deflected. In particular, the light ray entering the camera at an angle ϕ_0 from the horizontal originates from a different location on the screen. The apparent displacement, $\triangle z$, of the image is given by

$$
\begin{aligned}
\triangle z = &-\frac{1}{2}\gamma \triangle N^2 L_w^2 \\
&- \frac{n_w}{n_b}\gamma \triangle N^2 L_w L_b \\
&- \gamma \triangle N^2 L_w L_d \\
&- \frac{n_w}{n_p}\gamma \triangle N^2 L_w L_p \\
&- \frac{n_w}{n_a}\gamma \triangle N^2 L_w l_s
\end{aligned}
\tag{2.10}
$$

We can rearrange 2.10 to get change in buoyancy frequency squared $\triangle N^2$ in terms of the apparent displacement $\triangle z$

$$\triangle N^2 = -\frac{\triangle z}{L_w \gamma}\left(\frac{1}{2}L_w + \frac{n_w}{n_b}L_b + L_d + \frac{n_w}{n_p}L_p + \frac{n_w}{n_a}L_s\right)^{-1} \tag{2.11}$$

2. Laboratory measurement of apparent displacement:

   When internal gravity waves pass through the camera's field of view, the isopycnal surfaces are disturbed and thus the light ray passing through the medium is deflected. This is recorded by the digital camera as a sequence of images. We are interested in the apparent deflection of the horizontal black and white lines. When internal waves propagate in front of the black and white lines even the naked eye can notice the upper and lower edges of the black and white lines shifting up and down. In order to measure this apparent displacement field we need to study the change in intensity of an image with respect to another image recorded right after it in time. Let L_p and D_p be the length and depth pixel number of the digital images. The images recorded in the laboratory have pixel resolution of 964×1292 and thus the length and depth pixel pair (L_p,D_p) can range from $(0, 0)$ to $(963, 1291)$. Let the intensity of a perturbed image be given by $I(L_p, D_p)$ and the intensity of a perturbed image at a later time be $I'(L_p, D_p)$, then from [14] we have ,

$$\triangle z = (z_{-1} - z_0)\frac{(I' - I_0)(I' - I_1)}{(I_{-1} - I_0)(I_{-1} - I_1)} + (z_1 - z_0)\frac{(I' - I_0)(I' - I_{-1})}{(I_1 - I_0)(I_1 - I_{-1})} \tag{2.12}$$

   This equation helps us make the transition from pixel coordinates to real space coordinates. I_{-1}, I_0, and I_1 represent $I(L_p, Z_p - 1), I(L_p, Z_p)$, and $I(L_p, Z_p + 1)$. z_{-1}, z_0, and z_1 represent the depth of the pixels $Z_p - 1, Z_p$, and $Z_p + 1$.

2.4 Hilbert Transform

In this chapter we describe how to apply the Hilbert transform to internal waves in two dimensional fluids. The purpose of our experiments is to study the energetics of internal waves. In our lab we are trying to understand how mode-1 monochromatic internal waves propagate and interact with a vertical / sloping topography. Using synthetic schlieren technique we measure time rate of change of squared buoyancy frequency of the internal waves N_t^2. N_t^2 allowing us to quantify the energy flux. These measurements help us bring into focus the different mechanisms of propagation and reflection of internal gravity waves. It would be more useful if we could separate waves that are travelling towards the vertical end wall / slope from waves that are reflected from it. To separate out waves travelling in different directions but having the same frequency we use a technique called the Hilbert transform [5].

2.4.1 Hilbert transform for 2-dimensional waves

1. Definition

   We define Hilbert transform as a linear operator that takes a real function $f(t)$ and returns a complex function $z(t)$ whose real part is the input function such that $z(t) = f(t) + iy(t)$. Mercier et al, 2008 [5] used this technique to demodulate internal waves generated by an oscillating cylinder. The four beams generated by the oscillating cylinder experiment have different wavenumber but same frequency. They [5] demodulated these waves by their wave vector $\hat{\mathrm{k}}$ $= (k_x, k_z)$ according to the sign of the components k_x and k_z. We tried the same technique to demodulate mode-1 internal waves travelling right from their reflections travelling left. This is a modified adaptation of the technique used by [5]. Using Hilbert transform, Mercier et al (2008) were able to discriminate

2-dimensional internal waves generated by the vertically oscillating a cylinder in linearly stratified fluid that propagated in four different directions. We tried to apply the technique for our experiment where we want to discriminate mode-1 internal waves that were travelling towards the sloping topography from the ones that were reflected from it.

2. We do Hilbert transform on a wavefield that contains internal waves of a single frequency travelling in different directions . To operate on real experimental data involving 2 spatial dimensions, Hilbert transform can be computed in a few steps.

   (a) i. A Fourier transform in time of the field $U\,(x, z, t)$

   ii. A. In Fourier space, set the negative frequencies to zero so as to only keep the positive fundamental frequency $\omega = 2\pi f$, where f is the temporal frequency measured in hertz.

   B. This removes half the energy of the signal, we also multiply the resultant signal by a factor of two to preserve the amplitude of the signal.

   iii. The inverse Fourier transform generating the complex signal $\tilde{\mathrm{U}}(x, z, t)$.

   (b) Take the complex array $\tilde{\mathrm{U}}(x, z, t)$ and take a Fourier transform of the complex array in 3-dimensions (x, z, t).

   (c) In Fourier space the waves travelling in different spatial directions can be easily identified as they have unique signs of horizontal and vertical wavenumbers $\pm k_x, \pm k_z$. In our experiments, this complex resultant signal has four different waves in it.

$$\tilde{U} = \tilde{A}(x, z, t) + \tilde{B}(x, z, t) + \tilde{C}(x, z, t) + \tilde{D}(x, z, t) \tag{2.13}$$

with

$$\tilde{A}(x,z,t) = A(x,z,t)e^{i(k_x x + k_z z - \omega t)} \tag{2.14}$$

$$\tilde{B}(x,z,t) = B(x,z,t)e^{i(k_x x - k_z z - \omega t)} \tag{2.15}$$

$$\tilde{C}(x,z,t) = C(x,z,t)e^{i(-k_x x + k_z z - \omega t)} \tag{2.16}$$

$$\tilde{D}(x,z,t) = D(x,z,t)e^{i(-k_x x - k_z z - \omega t)} \tag{2.17}$$

Its important to notice that though the four waves oscillate in time at the same frequency ω, they do not propagate in the same direction which we can identify because of the different signs in front of the wave numbers k_x and k_z. The amplitudes of 2.13−2.16 depend on space and time, but the scales on which they vary must be much larger than the scales $\omega^{-1}, k_x^{-1}, k_z^{-1}$, around which the demodulation is performed.

(d) We can isolate the four waves 2.13−2.16 from each other. To do so we apply a filter in Fourier space, in the wavenumber directions: k_x and k_z associated with spatial directions x and z. The goal of this additional filtering is to only select positive or negative wavenumbers. We could apply a more selective filter to remove other wavenumbers.

(e) Do the inverse Fourier transform in all 3 dimensions to get back the original data. The resultant is complex.

3. Apply a uniform smoothing filter along the time axis to smooth the Hilbert transform.

2.4.2 Hilbert transform example: Oscillating cylinder experiment

We applied our Hilbert transform algorithm on the classical oscillating cylinder experiment [8] to see if we could filter out the four beams of the St.Andrew's cross based on their wavenumbers. We compared our results to the example given in [5] to know if our algorithm worked well. The oscillating cylinder experiment was realized in the laboratory in a Plexiglas tank of dimensions 488cm $\times$ 56cm $\times$ 46cm filled with linearly stratified salt water with buoyancy frequency $N = 0.95\text{s}^{-1}$. Quantitative internal wave measurements of density perturbations were made using synthetic schlieren technique. We apply the Hilbert transform on the N_t^2 field and try to separate out the four beams generated by the oscillating cylinder based on the sign of their wavenumber vector and the results are shown in figure 2.4 - 2.5.

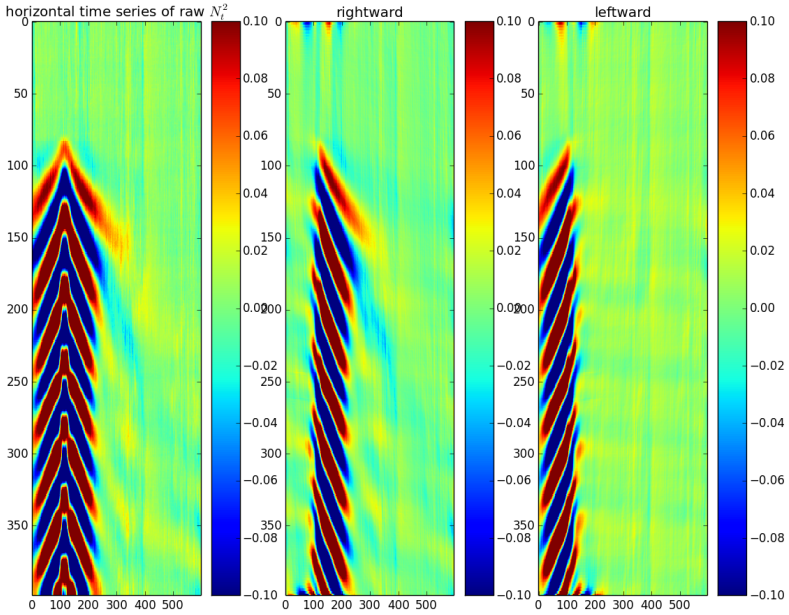

Figure 2.4: Figure a) shows the horizontal time series of N_t^2 field. Applying Hilbert transform on the horiontal time series, we filter out the internal waves generated by the oscillating cylinder into waves travelling b) rightward and c) leftward.

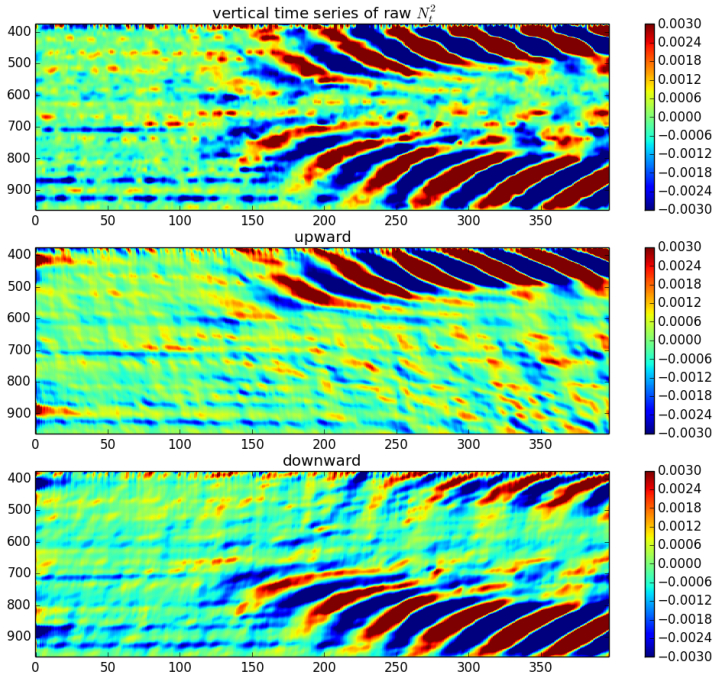

Figure 2.5: Figure a) shows the vertical time series of N_t^2 field. Applying Hilbert transform on the vertical time series, we filter out the internal waves generated by the oscillating cylinder into waves travelling b) upward and c) downward.

Chapter 3

Results

Our objective is to study the energetics of internal waves in linearly stratified fluid to be able to understand how internal waves propagate and reflect off a vertical end wall / sloping topography. Internal waves are capable of transporting momentum over large distances and hence its important to understand their mechanisms but its very hard to observe them in the ocean and that is one of the challenges involved in studying internal waves. The laboratory experiments and the experimental considerations are described in great detail in the previous chapters and in this chapter we present the results of those experiments.

3.1 Experimental results: mode-1 Internal wave generator

The experimental results are presented for the experiments that we have conducted. Every experiment that we consider has a stratification profile that is measured at the beginning of an experiment. The buoyancy frequency N, for experiments conducted are in the range 0.6 - 1 s^{-1}. The frequency ω, of the wave generator is usually in the

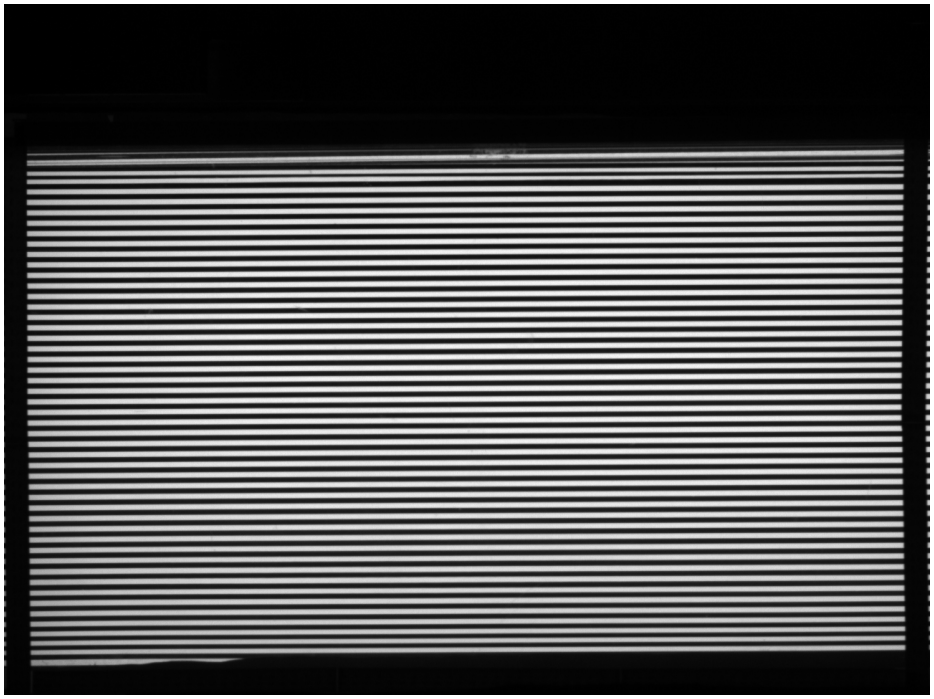

Figure 3.1: A single raw image in the sequence of images recorded for an experiment. This is the window in which a video of an experiment is recorded.

range 0.21 - 0.628 s^{-1}. We also consider the dimensionless ratio, ω/N, which for our experiments lie in the range 0.2 - 0.9. A frame in the video recorded for an experiment is shown in figure 3.1. The illuminated screen consisting of the black and white lines is a flat screen TV which is right behind the tank. The surface of the water is just below the black and white lines but the bottom of the tank cannot be seen in the window.

3.1.1 Case 1: No slope

Experimental specifics about experiments of type case-1 are given in table 3.1. Mode-1 internal waves are generated and are rightward propagating waves which propagate along the length of the tank and on the other end of the tank we have a vertical wall upon which internal waves reflect off and begin to propagate leftward.

Let us discuss the results of an experiment where the wave generator is set to a fre-

Table 3.1: Experimental parameters for no-slope.

Experiment ID	Period (s)	N (s^{-1})	ω (s^{-1})	Case
579	17	0.895	0.370	1
583	13	0.899	0.483	1
584	17	0.931	0.370	1
586	15	0.927	0.419	1
587	14	0.896	0.449	1
589	17	0.958	0.370	1
751	20	0.660	0.314	1
752	15	0.656	0.418	1
753	30	0.792	0.210	1
754	30	0.794	0.210	1
755	20	0.798	0.314	1
756	15	0.799	0.418	1
757	12	0.837	0.523	1
758	12	0.826	0.523	1
759	11	0.836	0.571	1
760	10	0.829	0.628	1

quency, ω=0.523 s^{-1} and the tank has a measured buoyancy frequency, N=0.837 s^{-1}. Figure 3.2 shows the stratification profile of the tank with depth. The temperature-conductivity probe detects a sharp jump in density at the surface of the water while descending to the bottom of the tank making it easy to track the position of the probe once it is inside the stratified fluid.

Figure 3.3 shows a vertical time series of N_t^2 of the experiment whose stratification profile is shown in figure 3.2.

The theoretical predictions for the experiment are given in the table 3.2 and sorted by the ratio ω/N.

Figure 3.4 is the N_t^2 field at a given instant of time. The figure clearly illustrates the vertical structure of the mode-1 internal waves. The surface of the water is clearly visible and we can observe there is about 2cm of mixed layer which can also be inferred

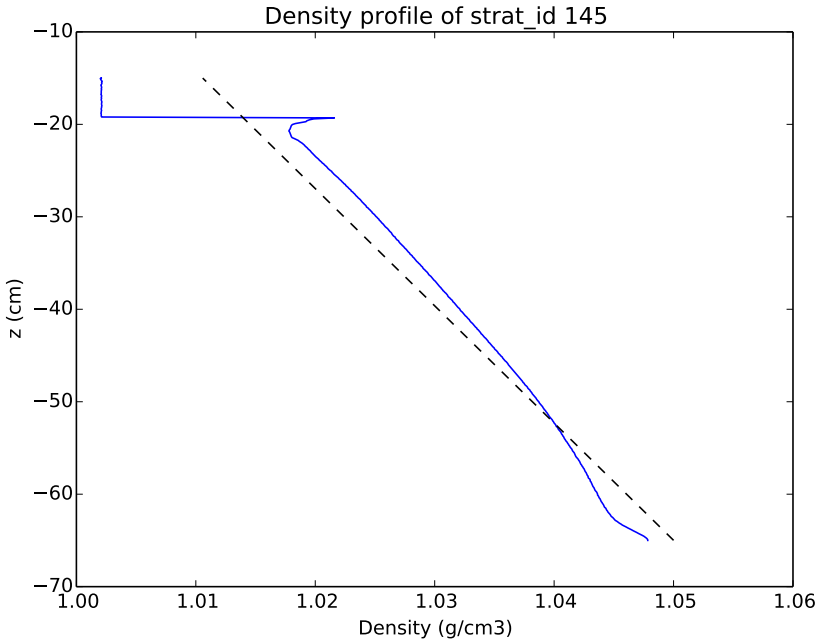

Figure 3.2: The vertical stratification profile of the tank before an experiment.

Table 3.2: Case 1: Theoretical predictions

Experiment ID	$\frac{\omega}{N}$	λ_x (cm)	C_{gx} ($\mathrm{m\,s^{-1}}$)
579	0.413	225	11.1
583	0.537	165	9.2
584	0.397	233	11.7
586	0.452	200	10.7
587	0.501	172	9.3
589	0.386	242	12.2
753	0.265	368	11.5
754	0.264	369	11.5
755	0.393	247	10.6
751	0.476	184	7.1
756	0.523	169	8.5
757	0.625	124	6.3
758	0.633	121	6
752	0.637	117	4.6
759	0.691	104	5
760	0.757	85	3.7

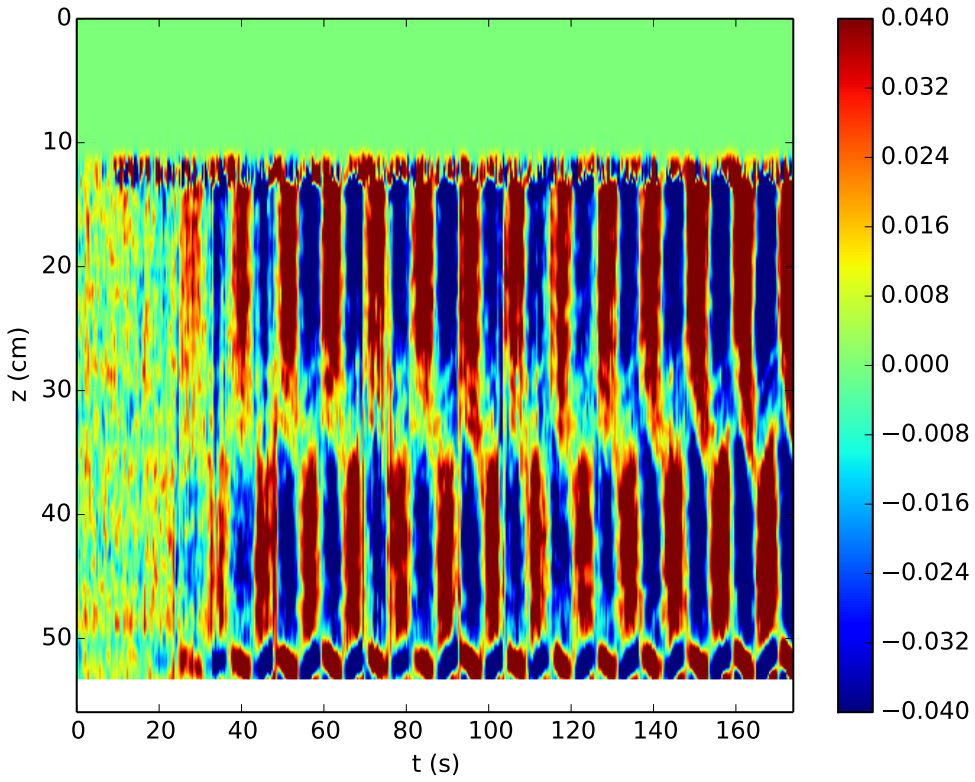

Figure 3.3: A vertical timeseries of N_t^2 of an experiment which has a forcing frequency of $\omega = 0.523$ s^{-1} and buoyancy frequency, N $= 0.837$ s^{-1}. The vertical timeseries is taken along a column in the middle of the camera window.

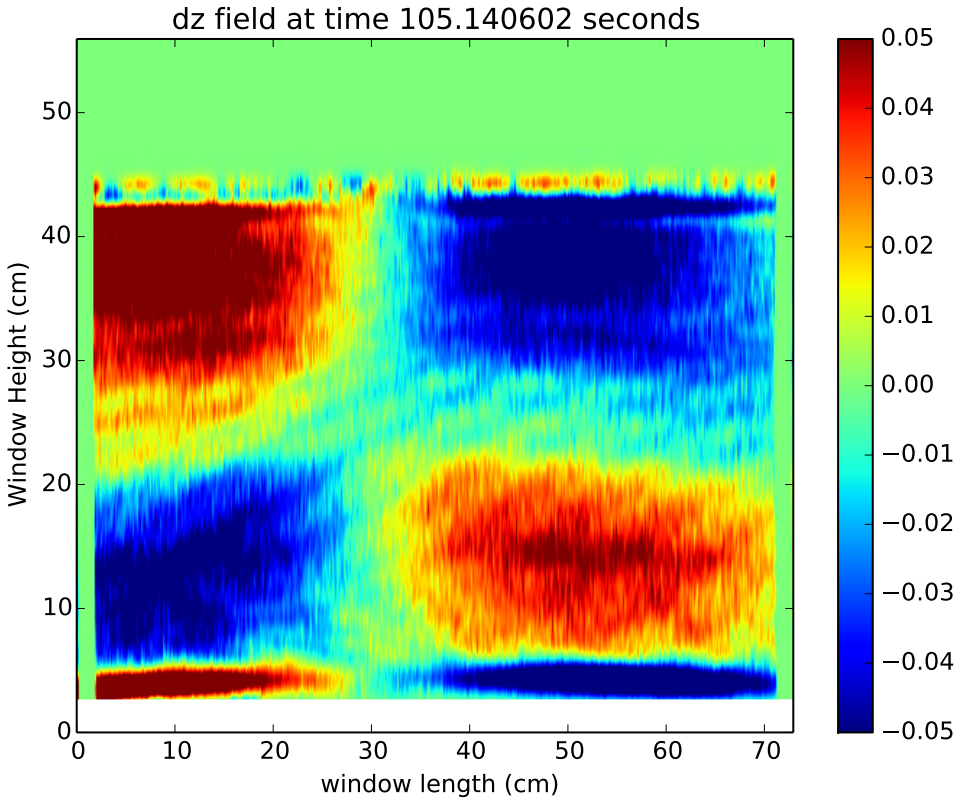

Figure 3.4: A snap shot in time where the internal waves propagate past the camera window but before it reflects back, of the N_t^2 field of an experiment which has a forcing frequency of $\omega = 0.523\text{s}^{-1}$ and buoyancy frequency, $N = 0.837\text{s}^{-1}$.

from the vertical stratification profile.

We can measure the horizontal displacement amplitude from the N_t^2 field. The horizontal displacement field is denoted by ς and is a way to measure the internal wave amplitude. A vertical time series of the horizontal displacement amplitude for an experiment is given in the figure 3.3. The camera starts recording $\sim 5 - 10$ s before the wave generator is switched on. In the figure 3.3 we can approximately see when the wave generator is switched on which is denoted by the surface disturbance in the time series. The vertical time series is taken at a column which in the middle of the rectangular window that is seen by the camera. In the time series we can see

that the wave generator gets switched on at about 8 seconds (seen from the surface disturbance) and the first internal wave appears at 22 s which is 14 s after the wave generator is switched on. The distance between the column where we take the time series is about 132.25 cm from the wave generator and thus the group speed of the internal wave is 9.45 $\mathrm{cm\,s^{-1}}$ as measured experimentally. We can compare it to the theoretically group speed, C_{gx} of 6.3 $\mathrm{cm\,s^{-1}}$. From the time series we can verify the time period of the wave generator which from the figure appears to be 12 s.

Figure 3.5 is the horizontal time series of the horizontal displacement field taken along a row in the window at some depth below the surface of the fluid. The horizontal time series helps us estimate the experimental value of the wavelength in the x-direction, λ_x the phase speed, C_{px} of the internal waves. The blue and red region represent the crest and the trough of the wave. The experimentally measured phase speed of the wave, $C_{Px}(measured) = 8.96$ $\mathrm{cm\,s^{-1}}$ and the theoretically measured $C_{Px}(theory) = 10.96$ $\mathrm{cm\,s^{-1}}$. From the relation $C_{Px} = \omega/k_x$ we can estimate the horizontal wavenumber and hence the horizontal wavelength, $\lambda_x(measured) = C_{gx} \times 2\pi/\omega = 107.5$ cm. The theoretically predicted value of the horizontal wavelength, $\lambda_x(theory)$ is 124 cm.

Hilbert transform is most efficient in processing data when the input is in steady state in the dimensions along which we apply the hilbert transform. Input data for the hilbert transform algorithm is the raw N_t^2 field. To increase the efficiency of the hilbert transform algorithm, we split the input data $(time, row, column)$ in time into several chunks where each chunk is of length = 2 time periods in time $time\ period = 2\pi/(frequency\ of\ the\ wavegenerator)$. Though the complete input field changes a lot with time, when we split the data into smaller chunks we can assume the data within each chunk can be fairly consistent while its only 2 time periods long in time. We repeatedly split the data in time every 16 seconds in the time axis. We also select a depth range which we do based on the stratification profile of the tank

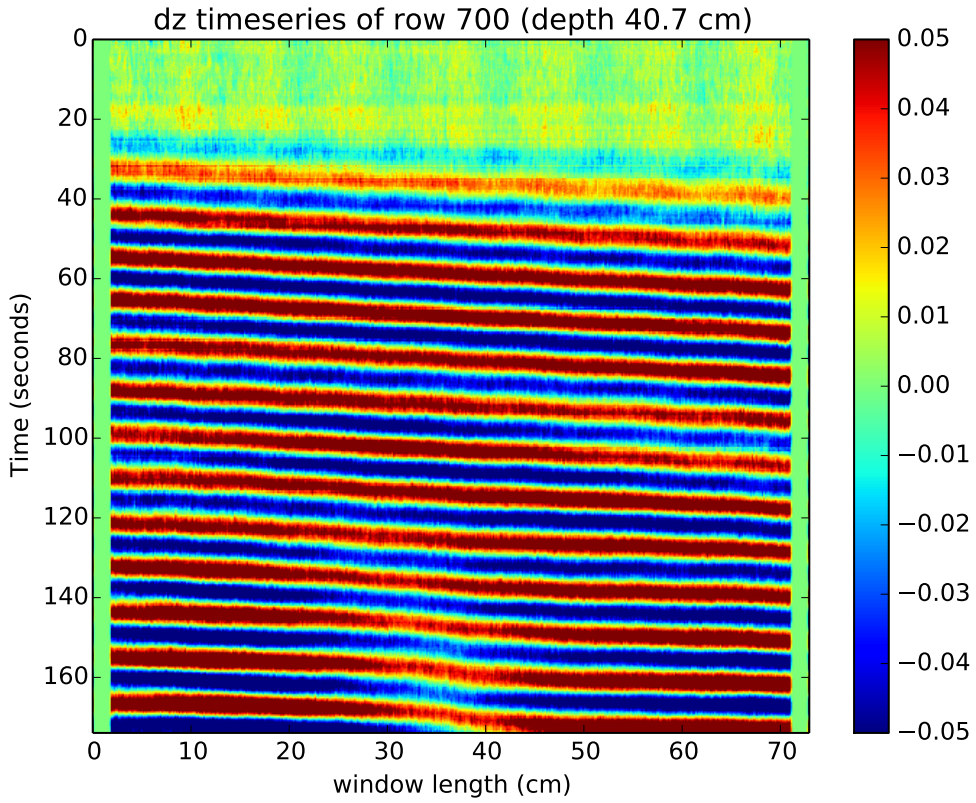

Figure 3.5: A horizontal time series of N_t^2 of an experiment which has a forcing frequency of $\omega = 0.523\text{s}^{-1}$ and buoyancy frequency, $N = 0.837\text{s}^{-1}$. The horizontal time series is taken along a row in the camera window where we observe the internal waves clearly.

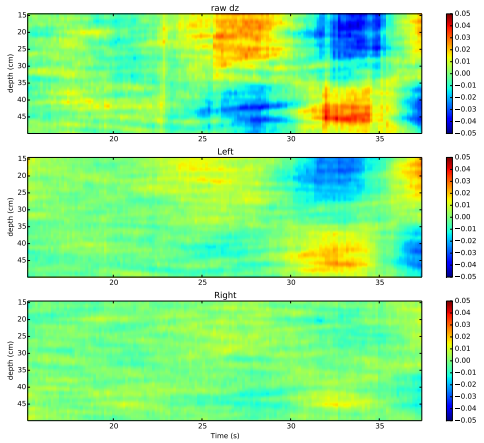

(a)

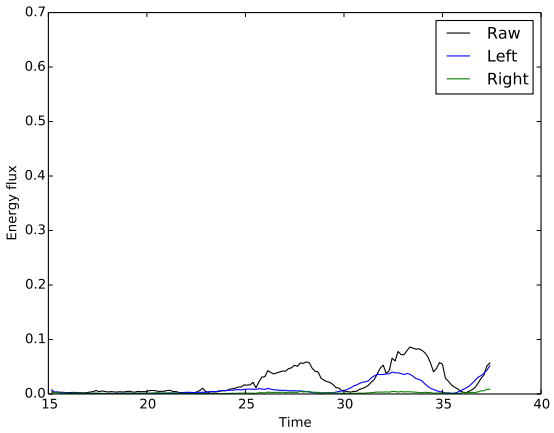

(b)

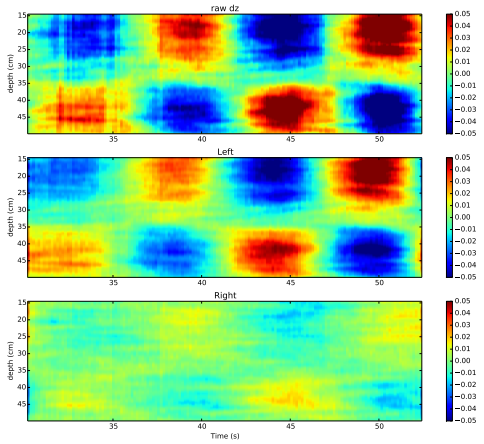

(c)

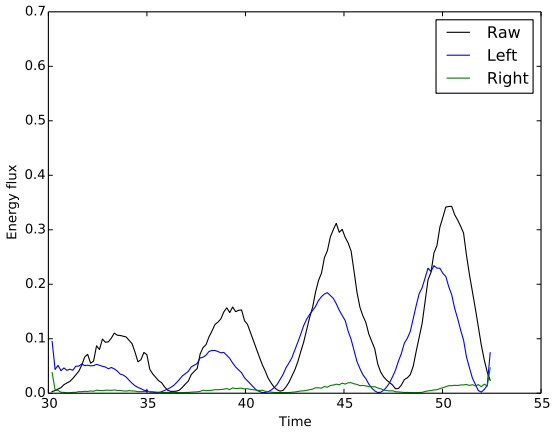

(d)

Figure 3.6: Figure a) and c) refer to experiments in case-1 : no-slope in a time window before reflected internal waves are observed. a) and c) are the vertical time series of (top) raw N_t^2 (middle) rightward propagating N_t^2 and (bottom) leftward propagating N_t^2.The plots b) and d) are the vertically averaged values of N_t^2 observed in the 3 subplots in a) and c) .

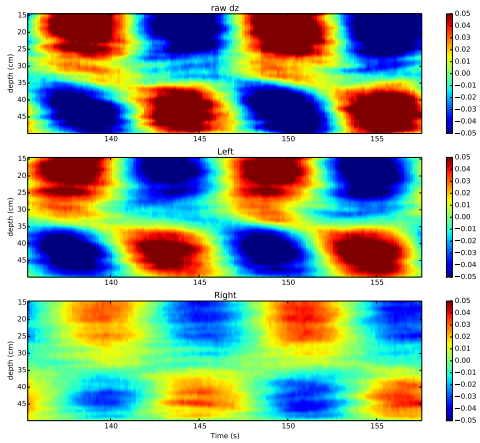

(a)

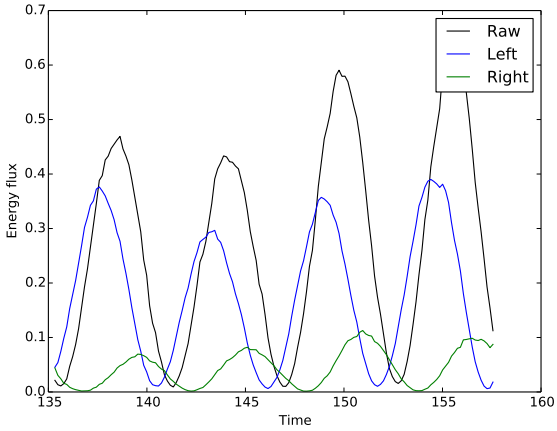

(b)

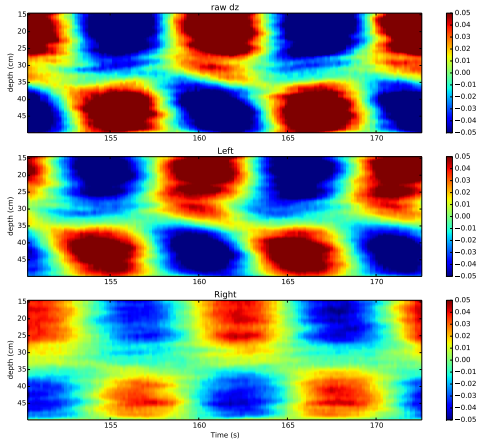

(c)

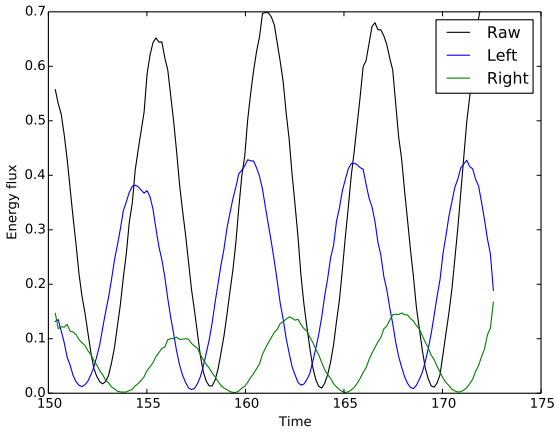

(d)

Figure 3.7: Figure a) and c) refer to experiments in case-1 : no-slope in a time window after reflected internal waves are observed. a) and c) are the vertical time series of (top) raw N_t^2 (middle) rightward propagating N_t^2 and (bottom) leftward propagating N_t^2.The plots b) and d) are the vertically averaged values of N_t^2 observed in the 3 subplots in a) and c)

for the experiment considered.

Figures 3.6 - 3.7c shown are the vertical time series of the horizontal energy flux $\langle F_{E_x} \rangle$ term derived from N_t^2 field where we take the vertical column in the center of the camera window. The three subplots in each figure refer to the $\langle F_{E_x} \rangle$ field : *i*) before applying the hilbert transform, *ii*) rightward propagating mode-1 internal wave retrieved from the hilbert transform and, *iii*) the reflected leftward propagating mode-1 internal wave retrieved from the hilbert transform. In the figure 3.6 we see the waves beginning to appear and we see only the rightward propagating wave. Although there is a small leftward propagating N_t^2 field in these figures, we can see that they are leaking from the rightward propagating wave when we apply hilbert transform. From the time series plots 3.7a - 3.7d we can see what appears to be the N_t^2 of mode-1 internal waves traveling leftward. Also we are able to measure N_t^2 field of the reflected waves appearing at approximately 115 s which is approximately equal to the estimated experimental reflection time of 106 s. The figures adjacent to the vertical time series plots are their respective vertically averaged N_t^2 of the raw, rightward and leftward propagating waves. It is worth noting that the N_t^2 of the reflected internal waves seem to be out of phase with the N_t^2 of the rightward propagating mode-1 internal wave.

The figure 3.6 is a plot of the vertically averaged horizontal energy flux $\langle \overline{F_{E_x}} \rangle$ of the raw, rightward and leftward propagating N_t^2. We can see that the hilbert transform applied to the input N_t^2 field has separated out the N_t^2 of rightward and leftward propagating internal waves.

We now look at the timeseries plot of vertically averaged energy flux $\langle \overline{F_{E_x}} \rangle$ field. $\langle \overline{F_{E_x}} \rangle$ of the raw, rightward and leftward propagating wave are shown in figure 3.8. From the figure we can see that initially there is no energy flux as we begin recording the experiment and after about 20 s the $\langle \overline{F_{E_x}} \rangle$ of raw and rightward internal waves

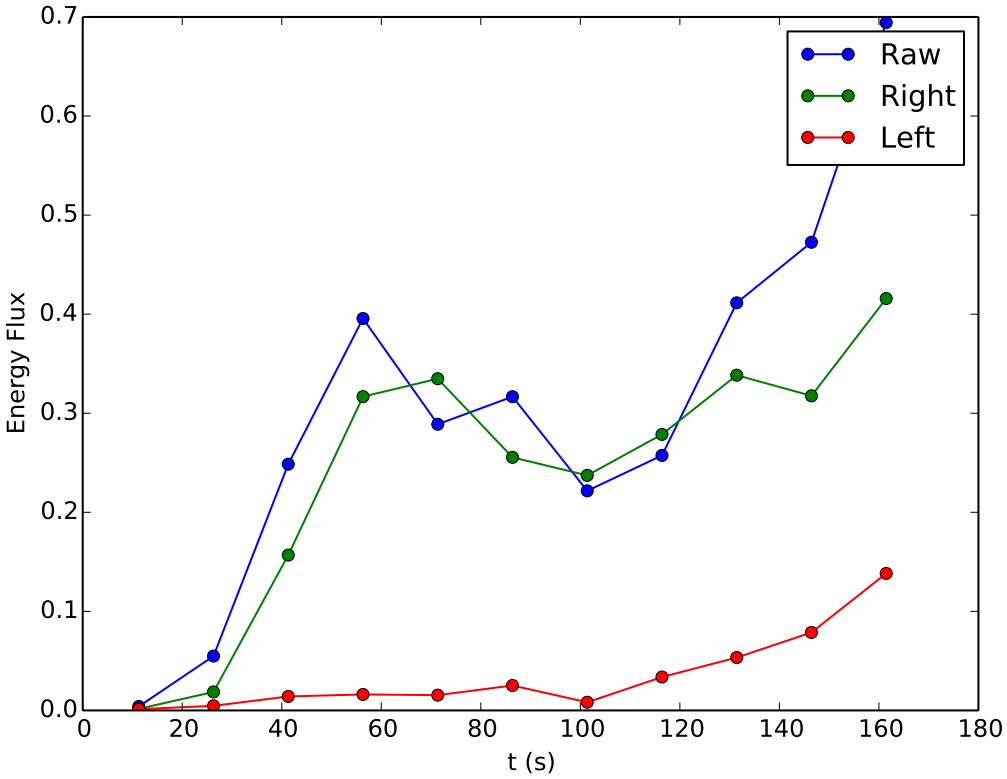

Figure 3.8: figure shows the timeseries of vertically averaged energy flux in x-direction $\langle\overline{F_{E_x}}\rangle$ of the raw, rightward and leftward propagating internal waves of an experiment in case-1: no slope.

rise together slowly till about 100 s till we encounter reflected internal waves. Once the $\langle\overline{F_{E_x}}\rangle$ of reflected internal waves starts increasing we can see a deviation in the $\langle\overline{F_{E_x}}\rangle$ of raw and rightward internal waves. This is because when the internal waves are generated, initially there are no reflections. The internal waves travel along the length of the tank and reflect back which takes about 100 s in this experiment. But it is possible for the $\langle\overline{F_{E_x}}\rangle$ of raw internal waves to either increase or decrease after encountering reflected internal waves depending on whether the waves are in phase or out of phase. So we need to keep that in mind while analyzing the experimental data.

Table 3.3: Experimental parameters for super-critical slope

Experiment ID	Period (s)	N (s^{-1})	ω (s^{-1})	Case	α	θ	$\frac{\alpha}{\pi/2-\theta}$
819	10	0.892	0.698	2	50	45	1.11
823	16	0.85	0.785	2	32	62	1.14
824	16	0.847	0.628	2	32	62	1.14
825	15	0.843	0.628	2	32	60	1.10

Table 3.4: Case 2: Theoretical predictions

Experiment ID	$\frac{\omega}{N}$	λ_x (cm)	C_{gx} ($m\,s^{-1}$)
819	0.704	100	5
823	0.462	188	9.1
824	0.464	172	8.6
825	0.497	187	9.1

3.1.2 Case 2: Supercritial slope

Let us consider experiments in which the internal waves propagate towards a sloping topography. Let the angle α be the angle between the sloping topography and the horizontal. The ratio $\alpha/(\frac{\pi}{2}-\theta) > 1$ if the slope is supercritical. If the slope is too large then the waves reflect upwards and away from the point attractor [13]. The rightward propagating waves encounter the supercritcal topography and reflect off. The experimental details of the experiments conducted with a subcritical slope are given in 3.3.

The theoretical predictions for the *case* 2 experiments are given in the table 3.4.

Figure 3.9 is the N_t^2 field at a given instant of time. The vertical structure of the N_t^2 field can be clearly identified as a mode-1 internal wave.

A vertical timeseries of the horizontal displacement N_t^2 field for this experiment is shown in figure 3.10. We can see reflected waves in the plot towards the end of the

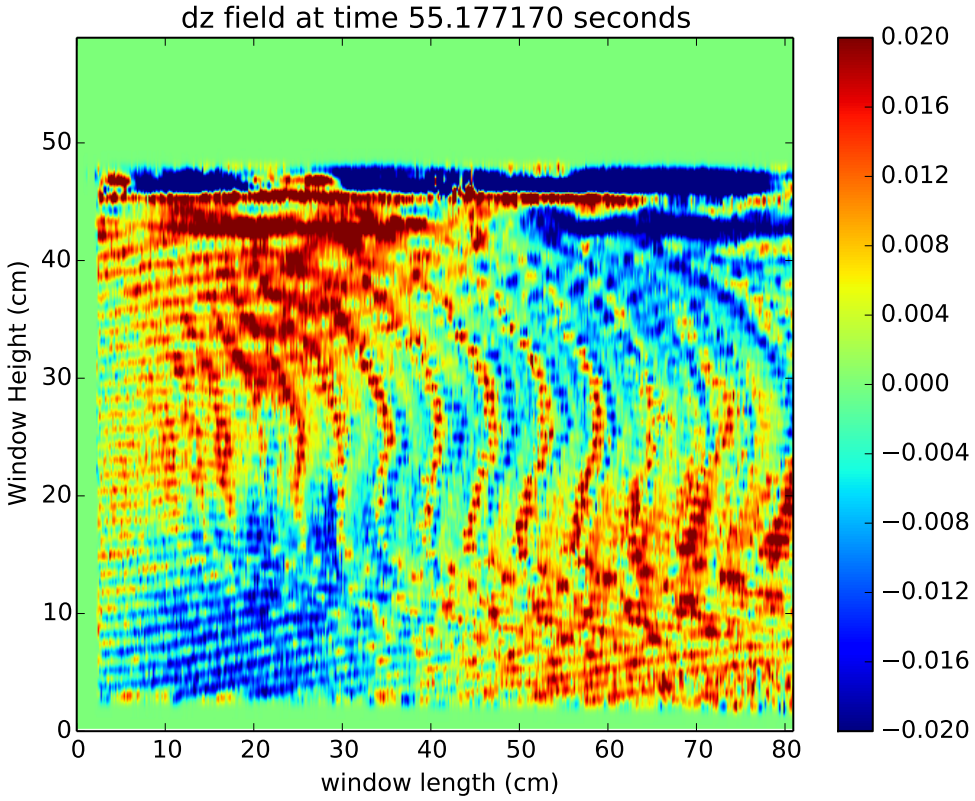

Figure 3.9: Snapshot of N_t^2 in time where the internal waves propagate past the camera window but before it reflects back, of the N_t^2 field of an experiment which has a forcing frequency of $\omega = 0.628\text{s}^{-1}$ and buoyancy frequency, $N = 0.892\text{s}^{-1}$.

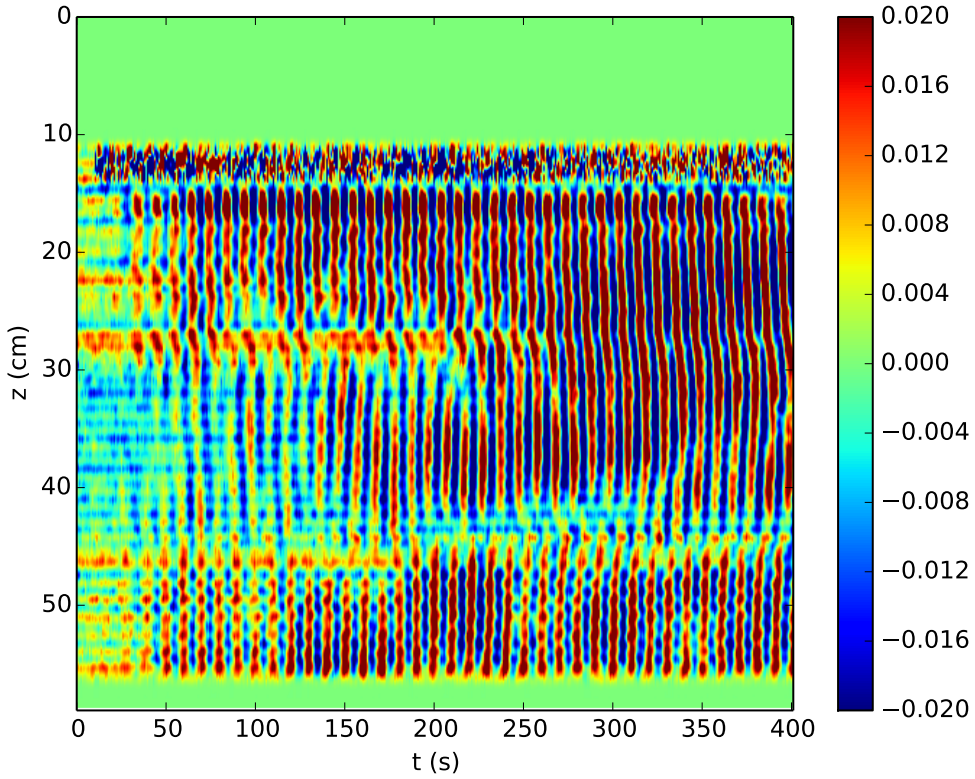

Figure 3.10: A vertical time series of N_t^2 of an experiment which has a forcing frequency of $\omega = 0.628\text{s}^{-1}$ and buoyancy frequency, $N = 0.892\text{s}^{-1}$. The vertical timeseries is taken along a column in the middle of the camera window.

timeseries.

Figure 3.11 is the horizontal time series of the horizontal displacement field taken along a row in the window at some depth below the surface of the fluid. The experimentally measured phase speed of the wave, $C_{Px}(measured) = 10.0\ \text{cm}\,\text{s}^{-1}$ and the theoretically measured $C_{Px}(theory) = 10.03\ \text{cm}\,\text{s}^{-1}$. From the relation $C_{Px} = \omega/k_x$ we can estimate the horizontal wavenumber and hence the horizontal wavelength, $\lambda_x(measured) = C_{gx} \times 2\pi/\omega = 100$ cm. The theoretically predicted value of the horizontal wavelength, $\lambda_x(theory)$ is 100 cm. Theory and observation match very well for this experiment.

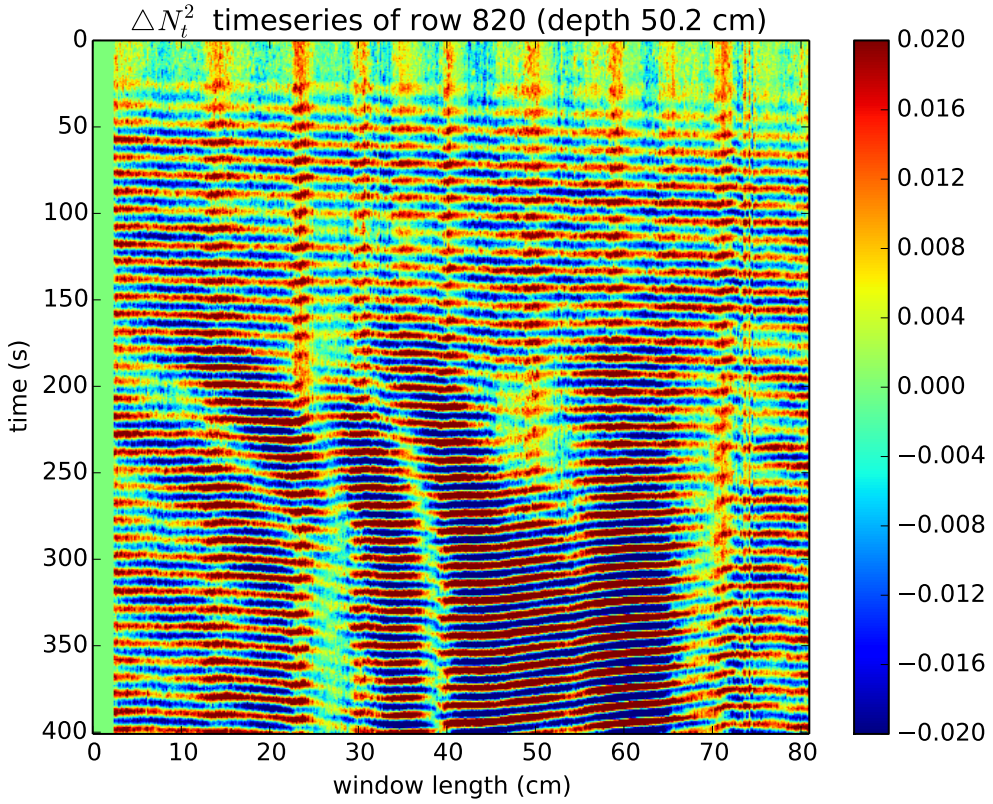

Figure 3.11: A horizontal time series of N_t^2 of an experiment which has a forcing frequency of $\omega = 0.628\text{s}^{-1}$ and buoyancy frequency, $N = 0.892\text{s}^{-1}$. The horizontal time series is taken along a row in the camera window where we observe the internal waves clearly.

The figure 3.12a - 3.12c shown are the vertical time series of the N_t^2 field for supercritical internal waves where we take the vertical column in the center of the camera window. The three subplots in each figure refer to the horizontal energy flux $\langle F_{E_x} \rangle$: *i*) before applying the hilbert transform, *ii*) rightward propagating mode-1 internal wave retrieved from the hilbert transform and, *iii*) the reflected leftward propagating mode-1 internal wave retrieved from the hilbert transform. The figures 3.17b- 3.17d refer to the vertically averaged horizontal energy flux $\langle \overline{F_{E_x}} \rangle$ of the raw, rightward and leftward propagating N_t^2 supercritical internal waves. The theoretical group speed for this experiment is $c_{gx} = 5$ cm s^{-1} and the experiment is run for a long time period so that reflections can be observed if present. From the vertical time series and the vertically averaged energy flux plot we can clearly see that there are reflected waves present. The reflected waves are out of phase with the rightward and the raw N_t^2 field.

We now look at the timeseries plot of vertically averaged energy flux $\langle \overline{F_{E_x}} \rangle$ field. $\langle \overline{F_{E_x}} \rangle$ of the raw, rightward and leftward propagating wave are shown in figure 3.13. From the figure we can see that the $\langle \overline{F_{E_x}} \rangle$ of raw and rightward propagating internal waves rise together after the waves have passed the vertical column where the measurements are taken. We start seeing reflected internal waves at about 100 s when we see the $\langle \overline{F_{E_x}} \rangle$ of the leftward internal waves rising. An interesting point to note regarding internal waves being in phase or out of phase with their reflection can be seen at about 230 s where we can see that the rightward and leftward propagating internal waves are out of phase with each other which is corroborated by the drop in $\langle \overline{F_{E_x}} \rangle$ of the raw internal waves.

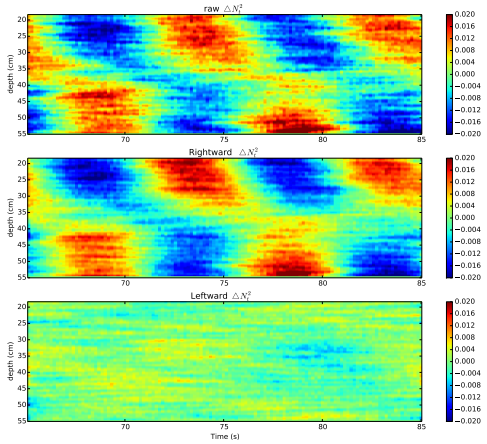

(a)

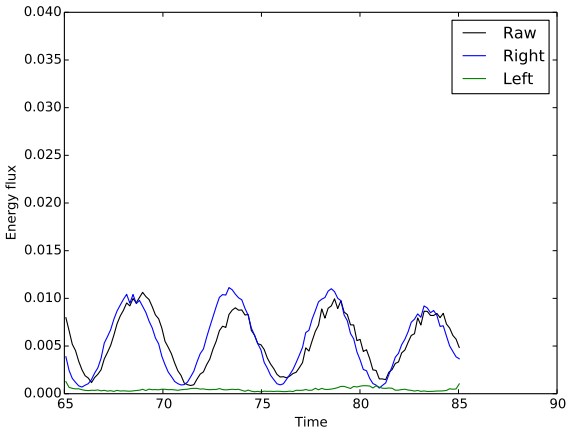

(b)

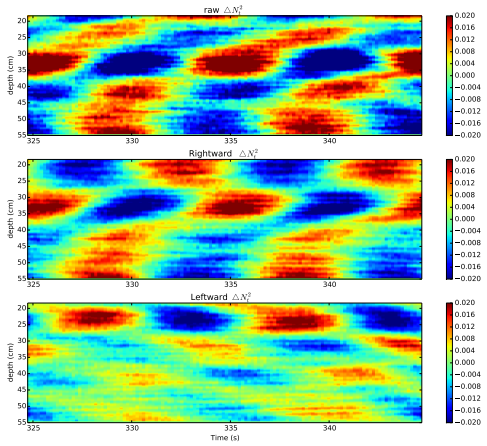

(c)

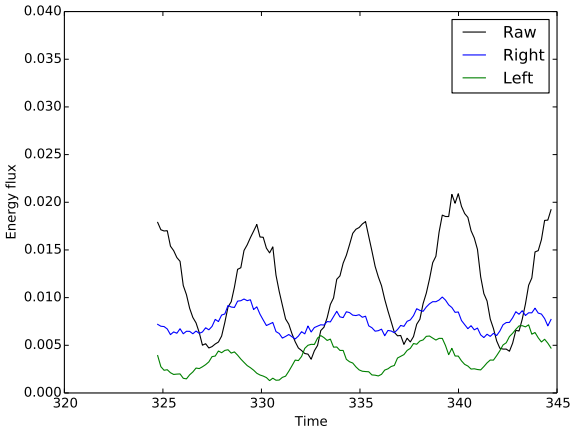

(d)

Figure 3.12: Figure a) and c) are the vertical time series of (top) raw N_t^2 (middle) rightward propagating N_t^2 and (bottom) leftward propagating N_t^2 internal waves of experiments in case 2: super-critical slope .Figure a) is in a time window before we observe reflected internal waves and c) is in a time window after we predict to see reflected internal waves. The plots b) and d) are the vertically averaged values of N_t^2 observed in the 3 subplots in a) and c) .

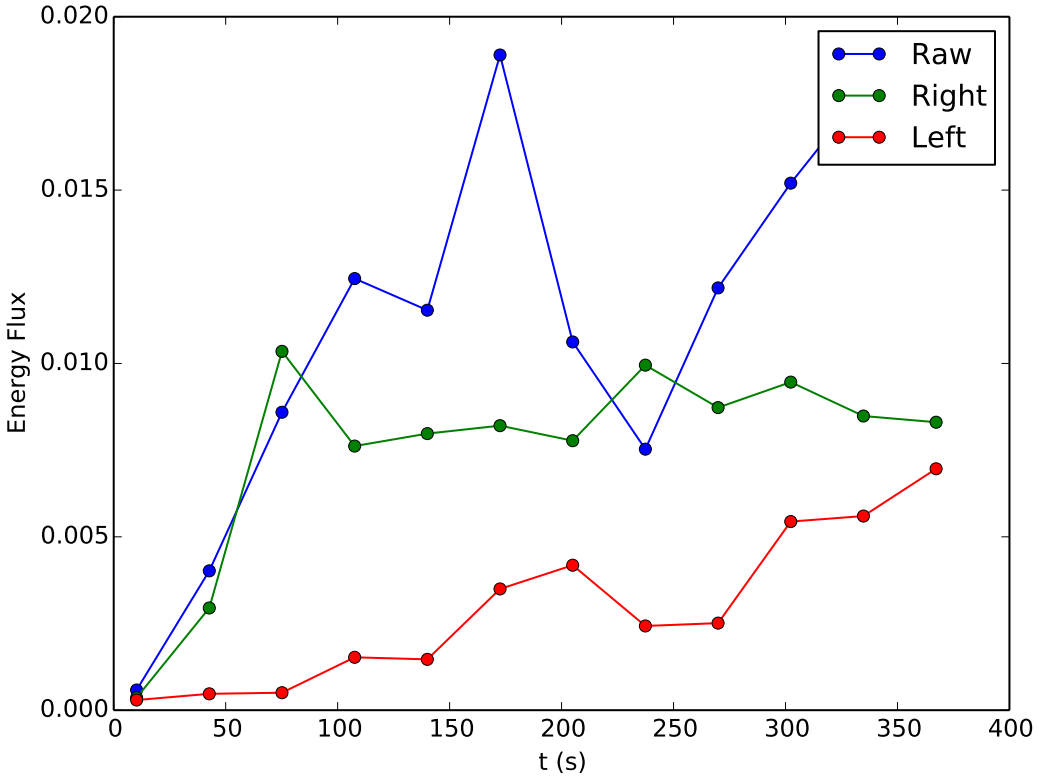

Figure 3.13: figure shows the timeseries of vertically averaged energy flux in x-direction $\langle \overline{F_{E_x}} \rangle$ of the raw, rightward and leftward propagating internal waves of an experiment in case-2: super-critical slope.

Table 3.5: Experimental parameters for sub-critical slope

Experiment ID	Period (s)	N (s^{-1})	ω (s^{-1})	Case	α	θ	$\frac{\alpha}{\pi/2-\theta}$
817	9	0.877	0.698	3	50	37	0.94
818	8	0.877	0.785	3	50	28	0.81
821	10	0.825	0.628	3	32	40	0.64
822	10	0.825	0.628	3	32	40	0.64

Table 3.6: Case 3: Theoretical predictions

Experiment ID	$\frac{\omega}{N}$	λ_x (cm)	C_{gx} ($m\,s^{-1}$)
817	0.795	75	3.1
818	0.895	49	1.2
821	0.761	84	3.5
822	0.761	84	3.5

3.1.3 Case 3: Subcritical slope

Let us consider the experiments in which the internal waves propagate towards a sloping topography. Let the angle α be the angle between the sloping topography and the horizontal. The ratio $\alpha/(\frac{\pi}{2}-\theta) < 1$ if the slope is subcritical. The details of the experimental set up are described in detail in Chapter 2. In theory, internal waves tend to wedge towards a point attractor when they reflect off a subcritical slope because they reflect alternatively from the sloping topography and the horizontal surface on the bottom. At the end of this path they dissipate [13]. The experimental details of the experiments conducted with a subcritical slope are given in 3.5

The theoretical predictions for *case* 3 experiments are given in the table 3.6.

Figure 3.14 is the N_t^2 field at a given instant of time. The vertical structure of the N_t^2 field can be clearly identified as a mode-1 internal wave.

A vertical timeseries of the horizontal displacement field N_t^2 for this experiment is

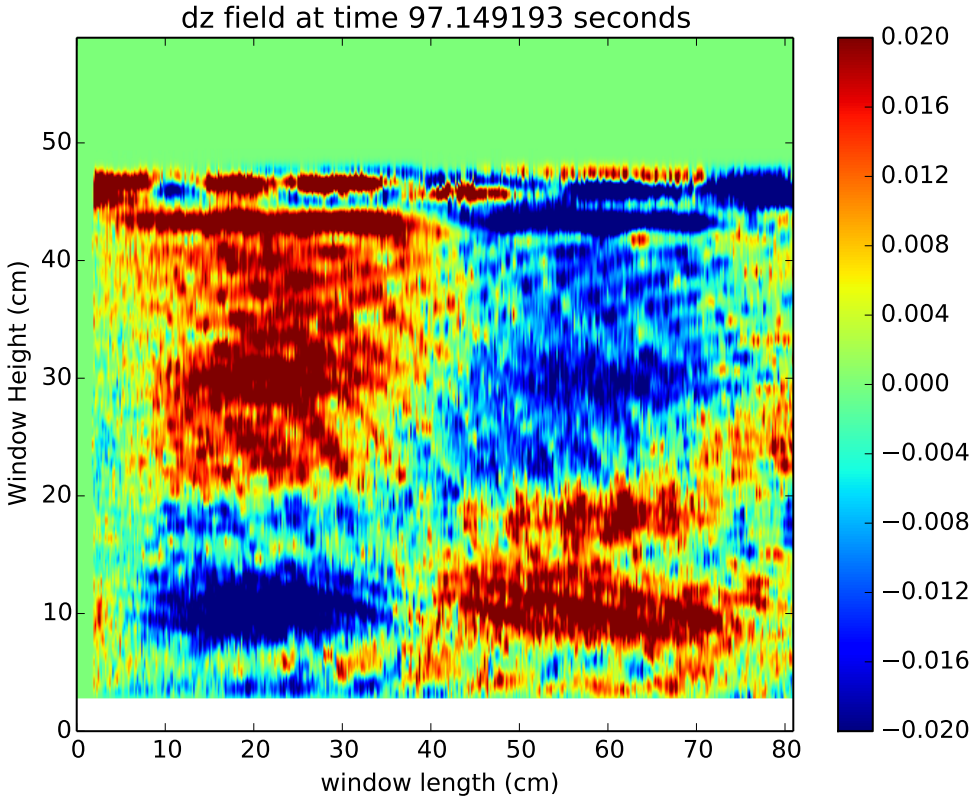

Figure 3.14: Snapshot of N_t^2 in time where the internal waves propagate past the camera window but before it reflects back, of the N_t^2 field of an experiment which has a forcing frequency of $\omega = 0.628\text{s}^{-1}$ and buoyancy frequency, $N = 0.825\text{s}^{-1}$.

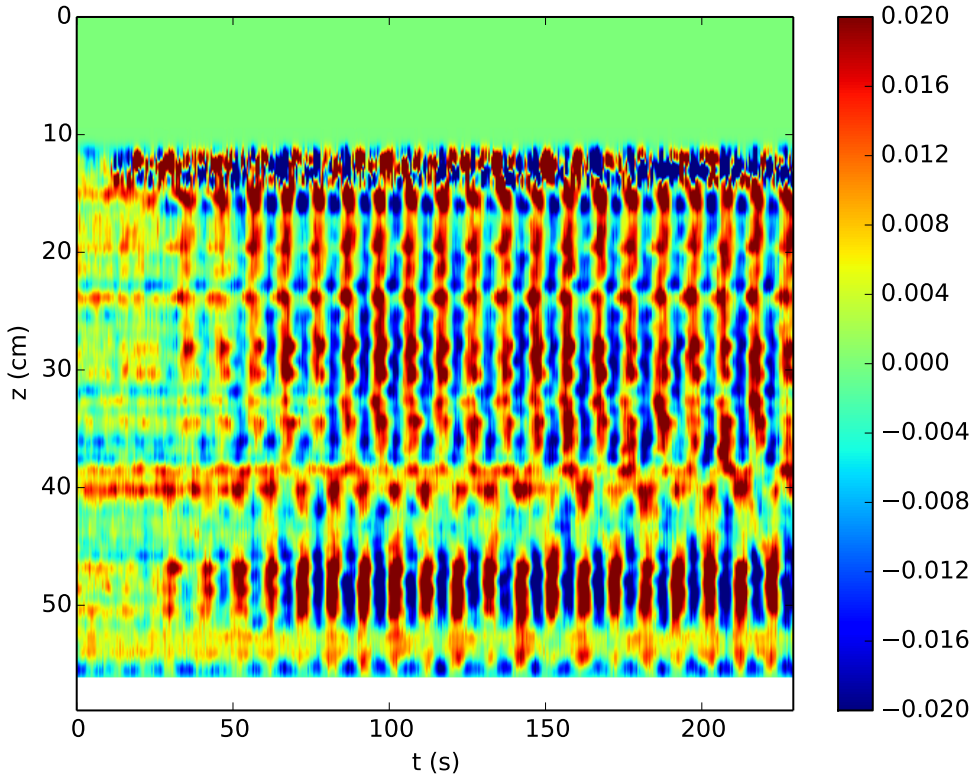

Figure 3.15: A vertical time series of N_t^2 of an experiment which has a forcing frequency of $\omega = 0.628\text{s}^{-1}$ and buoyancy frequency, $N = 0.825\text{s}^{-1}$. The vertical time-series is taken along a column in the middle of the camera window.

shown in figure 3.15

Figure 3.16 is the horizontal time series of the horizontal displacement field taken along a row in the window at some depth below the surface of the fluid. The experimentally measured phase speed of the wave, $C_{Px}(measured) = 10.0\ \text{cm}\,\text{s}^{-1}$ and the theoretically measured $C_{Px}(theory) = 10.03\ \text{cm}\,\text{s}^{-1}$. From the relation $C_{Px} = \omega/k_x$ we can estimate the horizontal wavenumber and hence the horizontal wavelength, $\lambda_x(measured) = C_{gx} \times 2\pi/\omega = 100$ cm. The theoretically predicted value of the horizontal wavelength, $\lambda_x(theory)$ is 100 cm. Theory and observation match very well for this experiment.

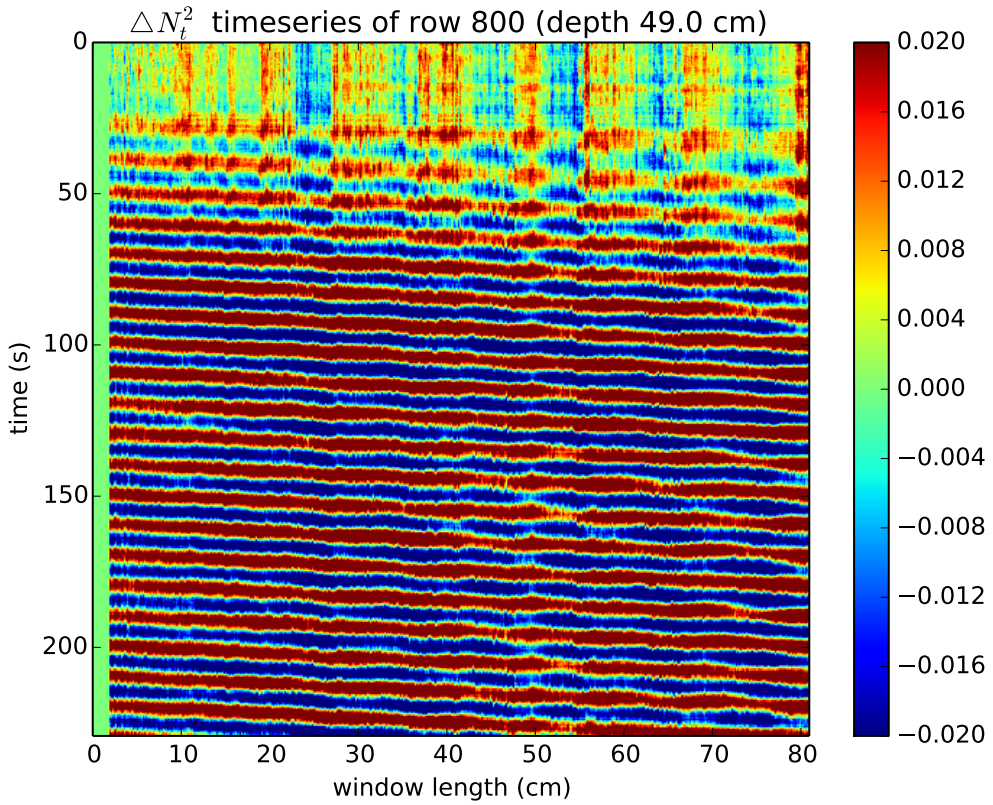

Figure 3.16: A horizontal time series of N_t^2 of an experiment which has a forcing frequency of $\omega = 0.628\text{s}^{-1}$ and buoyancy frequency, $N = 0.825\text{s}^{-1}$. The horizontal time series is taken along a row in the camera window where we observe the internal waves clearly.

The figure 3.17a - 3.17c shown are the vertical time series of the N_t^2 field for sub-critical internal waves where we take the vertical column in the center of the camera window. The three subplots in each figure refer to the horizontal energy flux $\langle F_{E_x} \rangle$: *i*) before applying the hilbert transform, *ii*) rightward propagating mode-1 internal wave retrieved from the hilbert transform and, *iii*) the reflected leftward propagating mode-1 internal wave retrieved from the hilbert transform. The figures 3.17b- 3.17d refer to the vertically averaged horizontal energy flux $\langle \overline{F_{E_x}} \rangle$ of the raw, rightward and leftward propagating N_t^2 sub-critical internal waves. The theoretical group speed for this experiment is $c_{gx} = 3.5$ cm s^{-1} and the experiment is run for a long time period so that reflections can be observed if present. From the vertical time series and the vertically averaged energy flux plot we can see that there are not reflected waves present.

We now look at the timeseries plot of vertically averaged energy flux $\langle \overline{F_{E_x}} \rangle$ field. $\langle \overline{F_{E_x}} \rangle$ of the raw, rightward and leftward propagating wave are shown in figure 3.18. As theory suggests when the slope is supercritical there should be no reflection and the figure also seems to suggest that there is no reflected internal waves.

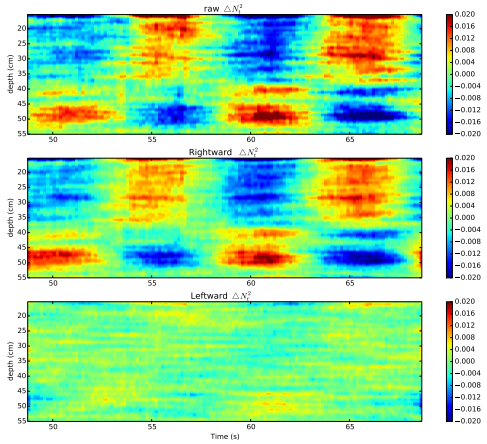

(a)

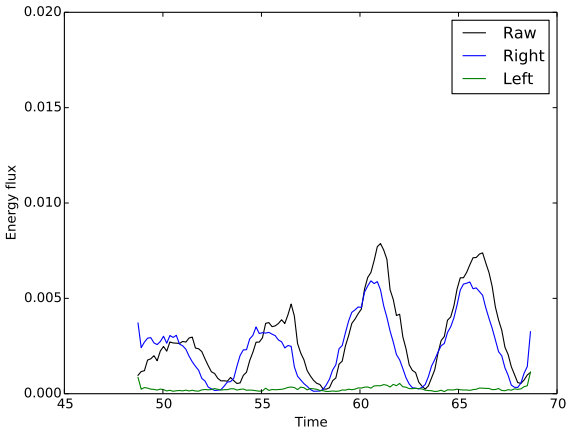

(b)

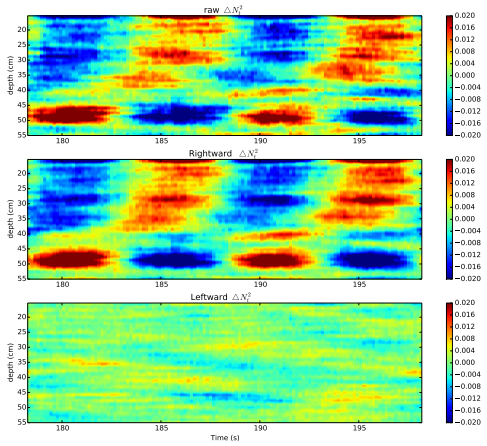

(c)

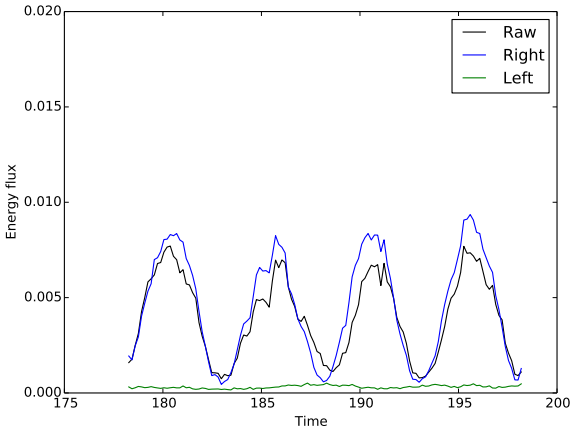

(d)

Figure 3.17: Figure a) and c) are the vertical time series of (top) raw N_t^2 (middle) rightward propagating N_t^2 and (bottom) leftward propagating internal waves N_t^2 of experiments in case 3: sub-critical slope .Figure a) is in a time window before we observe reflected internal waves and c) is in a time window after we predict to see reflected internal waves. The plots b) and d) are the vertically averaged values of N_t^2 observed in the 3 subplots in a) and c) .

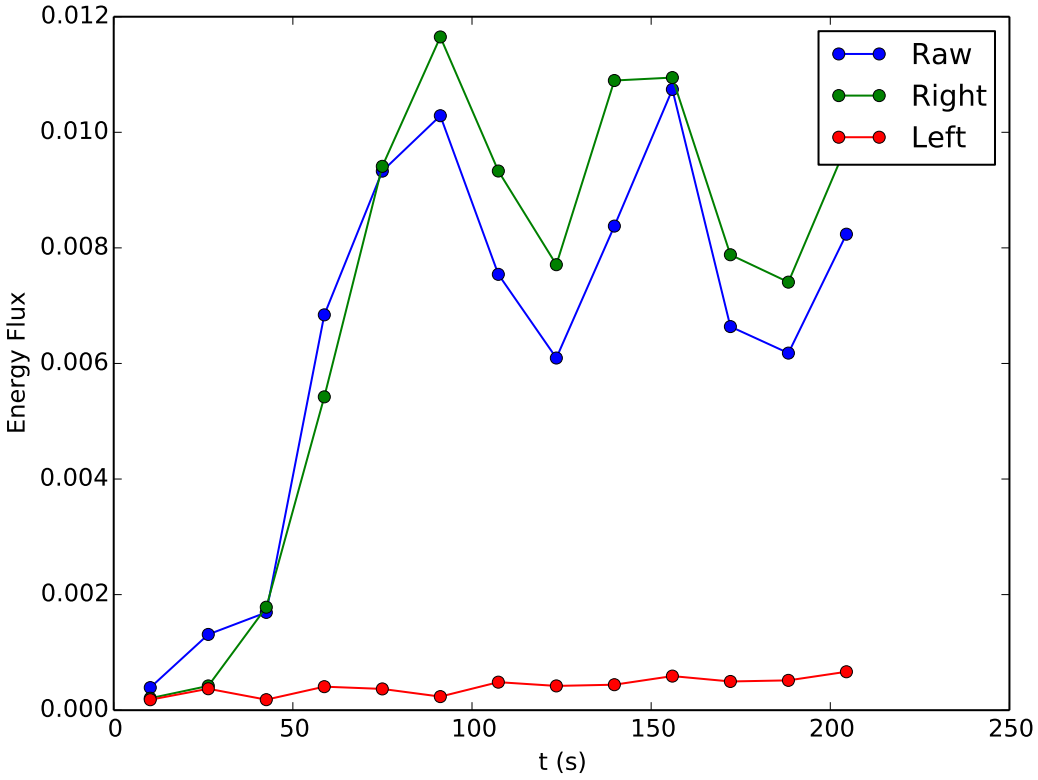

Figure 3.18: figure shows the timeseries of vertically averaged energy flux in x-direction $\langle \overline{F_{E_x}} \rangle$ of the raw, rightward and leftward propagating internal waves of an experiment in case-3: sub-critical slope.

Chapter 4

Conclusions and future work

As a preliminary step towards understanding how internal waves reflect off sloping topography such as the continental shelf, we performed a series of laboratory experiments to study the energy flux of propagating and reflecting internal waves in a continuously stratified salt water fluid. The internal waves are generated propagate along the length of the tank and reflect. The structure and amplitude of the internal waves are measured for different end boundary conditions. Using Hilbert transform we have separated the internal waves generated by the wavegenerator (traveling right) from the internal waves that are reflected from the end boundary (traveling left) enabling us to understand how much energy from the incoming waves is present in the reflected internal waves. The analysis of the energy flux of the internal waves during propagation and reflection using the Hilbert transform is helpful as it brings insight into phenomena that are difficult to observe during field studies. We have also tried to see how the internal waves generated dissipate and how much energy goes into mixing in our laboratory experiments. Our conclusions are presented in this section.

4.1 Conclusions

To measure internal waves we used a method called synthetic schlieren [14] to quantitatively measure internal waves generated in laboratory set up. But the formulations specified for the internal waves in the experiments were not applicable for our laboratory set-up. We modified it so that it was appropriate for our laboratory set-up so as to be able to accurately measure the change in squared buoyancy frequency of mode-1 internal waves for our laboratory settings.

Polarization relations for small amplitude vertically trapped mode-1 internal waves in linearly stratified fluid were derived for measuring the various parameters of the internal waves. Theory was associated to the quantitative measurements made using synthetic schlieren.

Based on [5] where Hilbert transform was used to separate internal waves with different wave vectors generated by an oscillating cylinder in stratified fluid, we developed a Hilbert trasform algorithm to separate mode-1 internal waves with different wave vectors. We applied Hilbert transform on mode-1 internal waves and are able to discriminate generated (rightward) propagating waves from their reflection.

Laboratory experiments were conducted to realize mode-1 internal waves and record their generation,propagation and reflection for 3 types of experiments that are distinct in their end wall boundary conditoin: No slope, subcritical slope and supercritical slope. We are able to measure and compare their properties such as time rate of change of squared buoyancy frequency of the internal waves ${N^2}_t$ defined by 1.55 from which we measure the vertically averaged horizontal energy flux $\langle\overline{F_{E_x}}\rangle$ defined by 1.64 of generated waves and reflected waves for all 3 types of experiments.

The polarization relations for mode-1 vertically trapped internal waves are given in table 4.1. Synthetic schlieren gives us quantitative measurements of the change in squared buoyancy frequency $\triangle N^2$ from which we can use the polarization relation to

get the horizontal displacement amplitude A_ς. Once we have A_ς field we can determine the basic fields where each of the fields have a magnitude and phase.

Table 4.1: Polarization relations and correlations between fields for small amplitude vertically trapped mode-1 internal waves in linearly stratified fluid.

Defining formula	Relationship to horizontal displacement	
ς	A_ς	$\varsigma = A_\varsigma \cos(k_z z)\sin(k_x x - \omega t)$
$u = \frac{\partial \varsigma}{\partial t}$	$A_u = -\iota\omega \cos(k_z z) A_\varsigma$	$u = -\omega A_\varsigma \cos(k_z z)\cos(k_x x - \omega t)$
$\frac{\partial w}{\partial x} = -\frac{\partial u}{\partial x}$	$A_w = -\frac{\omega k_x \sin(k_z z)}{k_z} A_\varsigma$	$w = -\frac{\omega k_x}{k_z} A_\varsigma \sin(k_z z)\sin(k_x x - \omega t)$
$\rho_0 \frac{\partial u}{\partial t} = -\frac{\partial p}{\partial x}$	$A_p = -\iota \frac{\rho_0 \omega^2 \cos(k_z z)}{k_x} A_\varsigma$	$p = -\frac{\rho_0 \omega^2}{k_x} A_\varsigma \cos(k_z z)\cos(k_x x - \omega t)$
$w = \frac{\partial \xi}{\partial t}$	$A_\xi = -\iota \frac{k_x \sin(k_z z)}{k_z} A_\varsigma$	$\xi = -\frac{k_x}{k_z} A_\varsigma \sin(k_z z)\cos(k_x x - \omega t)$
$\rho' = -\frac{\partial \rho}{\partial z}\xi$	$A_{\rho'} = -\iota \frac{k_x \rho_0 N^2 \sin(k_z z)}{g k_z} A_\varsigma$	$\rho' = -\frac{k_x \rho_0 N^2}{g k_z} A_\varsigma \sin(k_z z)\cos(k_x x - \omega t)$
$\triangle N^2 = -\frac{g}{\rho_0}\frac{\partial \rho}{\partial z}$	$A_{\triangle N^2} = -\iota k_x N^2 \cos(k_z z) A_\varsigma$	$\triangle N^2 = k_x N^2 A_\varsigma \cos(k_z z)\cos(k_x x - \omega t)$
$N_t^2 = \frac{\partial \triangle N^2}{\partial t}$	$A_{N_t^2} = k_x \omega N^2 \cos(k_z z) A_\varsigma$	$N_t^2 = k_x \omega N^2 A_\varsigma \cos(k_z z)\sin(k_x x - \omega t)$

Correlations

$$\langle F_{E_x} \rangle = \langle pu \rangle = \tfrac{1}{2}\frac{\rho_0 \omega^3}{k_x} A_\varsigma^2 \cos^2(k_z z)$$

$$\langle \overline{F_{E_x}} \rangle = \langle \langle pu \rangle_t \rangle_z = \tfrac{1}{4}\frac{\rho_0 \omega^3}{k_x} A_\varsigma^2$$

In Chapter 2, we showed that the components of phase speed $\vec{c_p} = (c_{px}, c_{pz})$ are not the same as the measured components of phase speed from a vertical time series $\vec{c_P} = (c_{Px}, c_{Pz})$. For all the experiments conducted, we measured the horizontal observed phase speed c_{Px}.

We are thus able to compare the observed c_{Px} and the theoretical values of c_{Px} and is shown in figure 4.1 as a scatterplot where we see how c_{Px} changes as ω/N goes from 0 to 1. In theory, c_{Px} has an exponential decay as ω/N goes from 0 to 1. The experimental observations also follow the same trend.

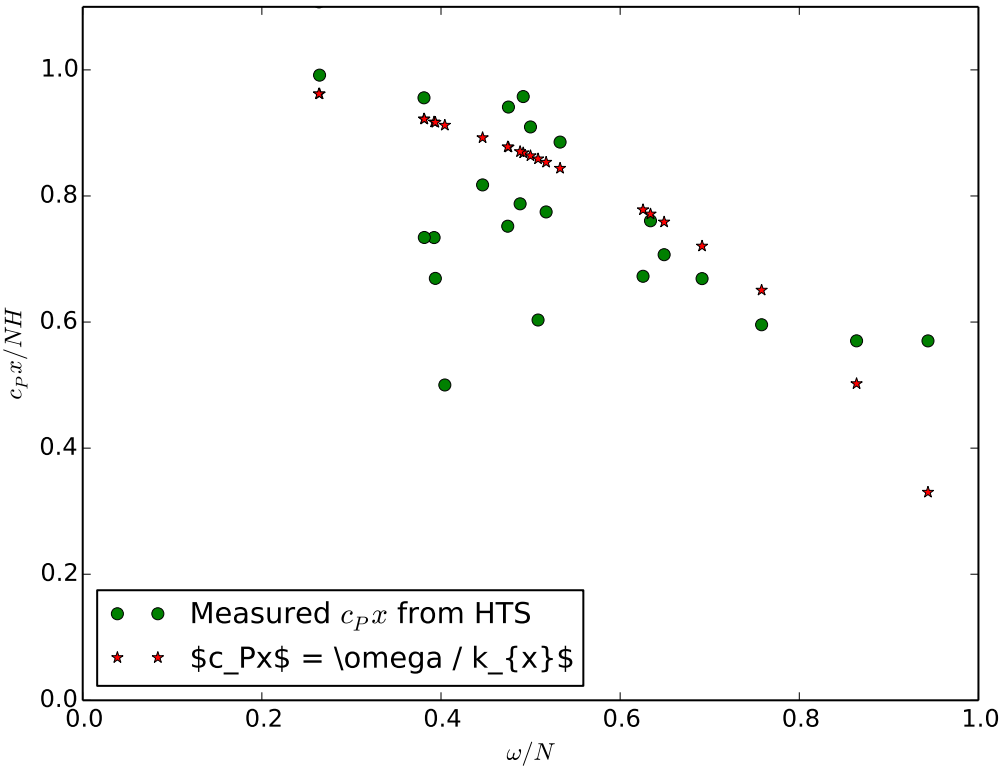

Figure 4.1: Figure shows a comparison of the theoretical c_{Px} and the observed c_{Px}. Each green circle refers to a single experiment in Case-1: no slope. The measurements are taken before we observe reflections. The red star is the theoretically predicted value of c_{Px} for the given ratio of ω/N.

Theoretically horizontal wavenumber 4.1 of mode-1 internal waves is derived from the dispersion relation 1.29. We can experimentally measure the horizontal wavenumber from the relation by measuring c_{Px} where $c_{Px} = \omega/k_x$. We then can look at how the theoretical k_x given by 4.1 compares with the observed k_x. A figure showing the comparison between the experimental and theoretical values of the horizontal

wavenumber is given in 4.2.

$$k_x = \frac{\omega k_z}{\sqrt{(N^2 - \omega^2)}} \tag{4.1}$$

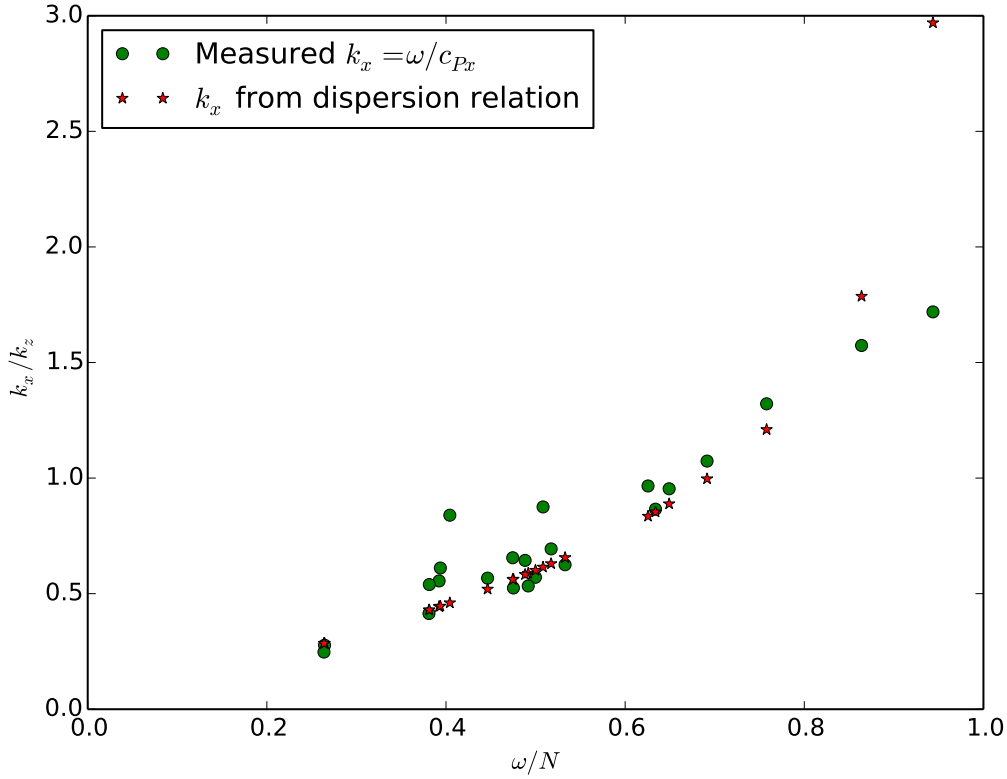

Figure 4.2: Fig shows a comparison of the theoretical k_x and the experimental k_x.Each green circle refers to a single experiment in Case-1: no slope. The measurements are taken before we observe reflections. The red star is the theoretically predicted value of k_x for the given ratio of ω/N

We measure the vertically averaged energy flux of the internal waves $\langle\overline{F_{E_x}}\rangle$ from the finite difference approximation to the time derivative of the squared buoyancy frequency, N_t^2 which we measure from synthetic schlieren for every experiment. We can look at how $\langle\overline{F_{E_x}}\rangle$ field changes before any reflections occur over several experiments as a function of ω/N. These experiments have the same wave generator amplitude. We

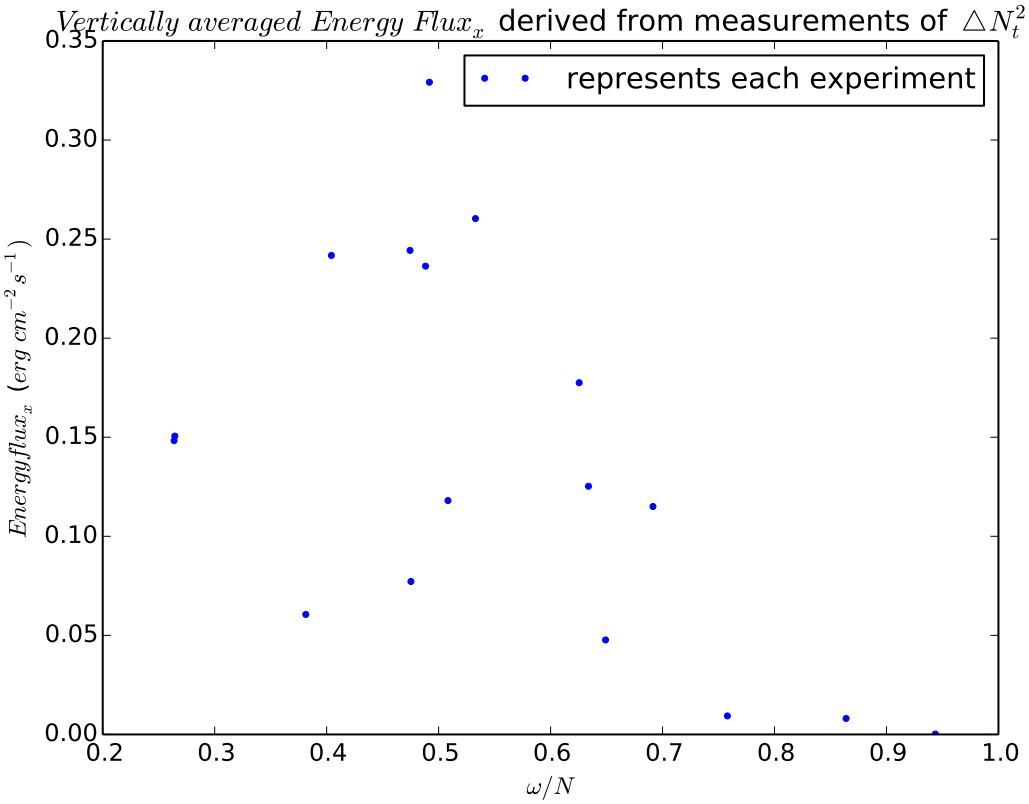

Figure 4.3: Figure shows the vertically averaged energyflux in x-direction, $\langle\overline{F_{E_x}}\rangle$ field of the raw mode-1 internal waves measured before reflected waves appear. Every blue dot refers to an experiment in case-1: no slope.

are only looking at the $\langle\overline{F_{E_x}}\rangle$ field averaged over the time period before the reflected internal waves begin to appear and is shown in figure 4.3.

Implementing Hilbert transform we are able to filter out propagating internal waves from reflected internal waves. We can look at $\langle\overline{F_{E_x}}\rangle$ field for raw internal waves and reflected internal waves. Let us consider experiments from Case 1: No slope shown in figure 4.4, Case 2: Supercritical slope shown in figure 4.4 and Case 3: Subcritical slope shown in figure 4.5. The last subplot in 4.6 gives information regarding the portion of energy that is reflected as a function of ω/N and maximum reflection occurs at $\omega/N = 0.5$. For case 1 experiments on average the reflected energy efficiency seems

to be around 20%. A trend across the range of ω/N is very hard to observe clearly and we need to do more experiments. In the figure for case 2 4.5 we see a very high reflected energy efficiency. But its harder to compare this to experiments from Case 1 as in the case of 4.4 the experiments has a wave generator amplitude of 4cm while the wave generator amplitude for experiments in 4.5 had a wave generator amplitude is 1 cm. Dissipation is directly proportional to wave amplitude. Theoretically we would expect maximum reflection efficiency in case 1 experiments than in case 2 experiments but since dissipation is higher in case 1 experiments we are seeing larger reflection efficiencies in experiments of type case 2 rather than case 1.

4.2 Future work

One of the important observations we have made are on the trends in horizontal phase velocity c_{Px} and the horizontal wavenumber k_x. It would be very useful to have additional experiments in the range ω/N as we don't have too many experimental points in the beginning and in the end of the range ω/N in figure 4.1.

We have succesfully separated out propagating mode-1 internal waves from its reflection to help quantify dissipation, i.e, to look at how $\langle\overline{F_{E_x}}\rangle$ field of the internal waves changes as we move along the camera window length. To make a more justified estimation of the reflected energy efficiency we need to realize additional experiments in case 2 and case 3.

We find that case 2 experiments have a higher reflection efficiency than case 1 experiments and we attribute this to the fact that the wave generator amplitude is larger for case 1 experiments thus it has a larger dissipation. This needs to be studied furthur by realizing additional experiments over the whole range of the ratio ω/N and the wave generator amplitude.

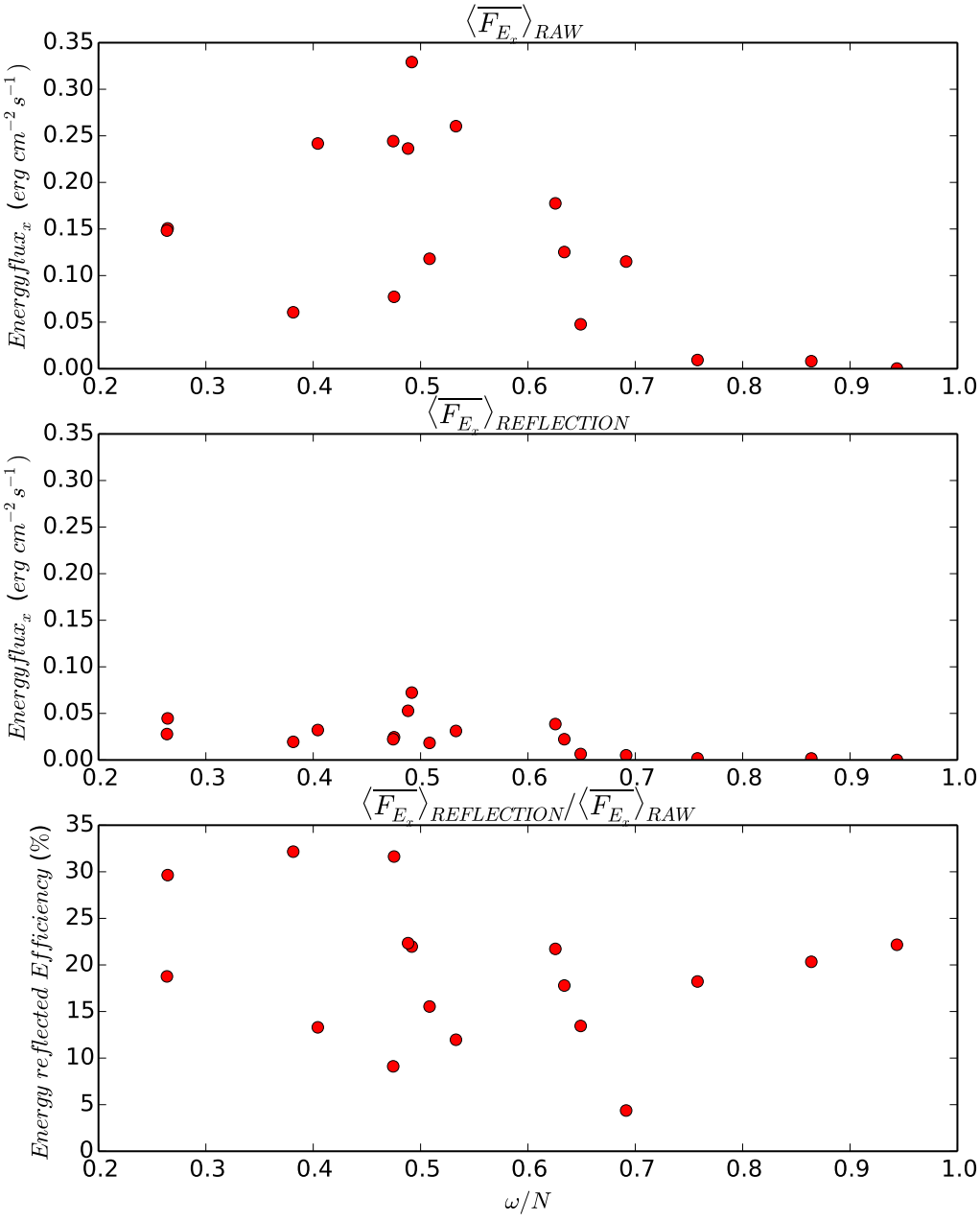

Figure 4.4: fig shows for case 1: no slope, a) $\langle\overline{F_{E_x}}\rangle$ field of raw internal waves, b) $\langle\overline{F_{E_x}}\rangle$ field of reflected internal waves and c) the ratio $\langle\overline{F_{E_x}}\rangle$ field of reflected internal waves/ $\langle\overline{F_{E_x}}\rangle$ field of raw internal waves

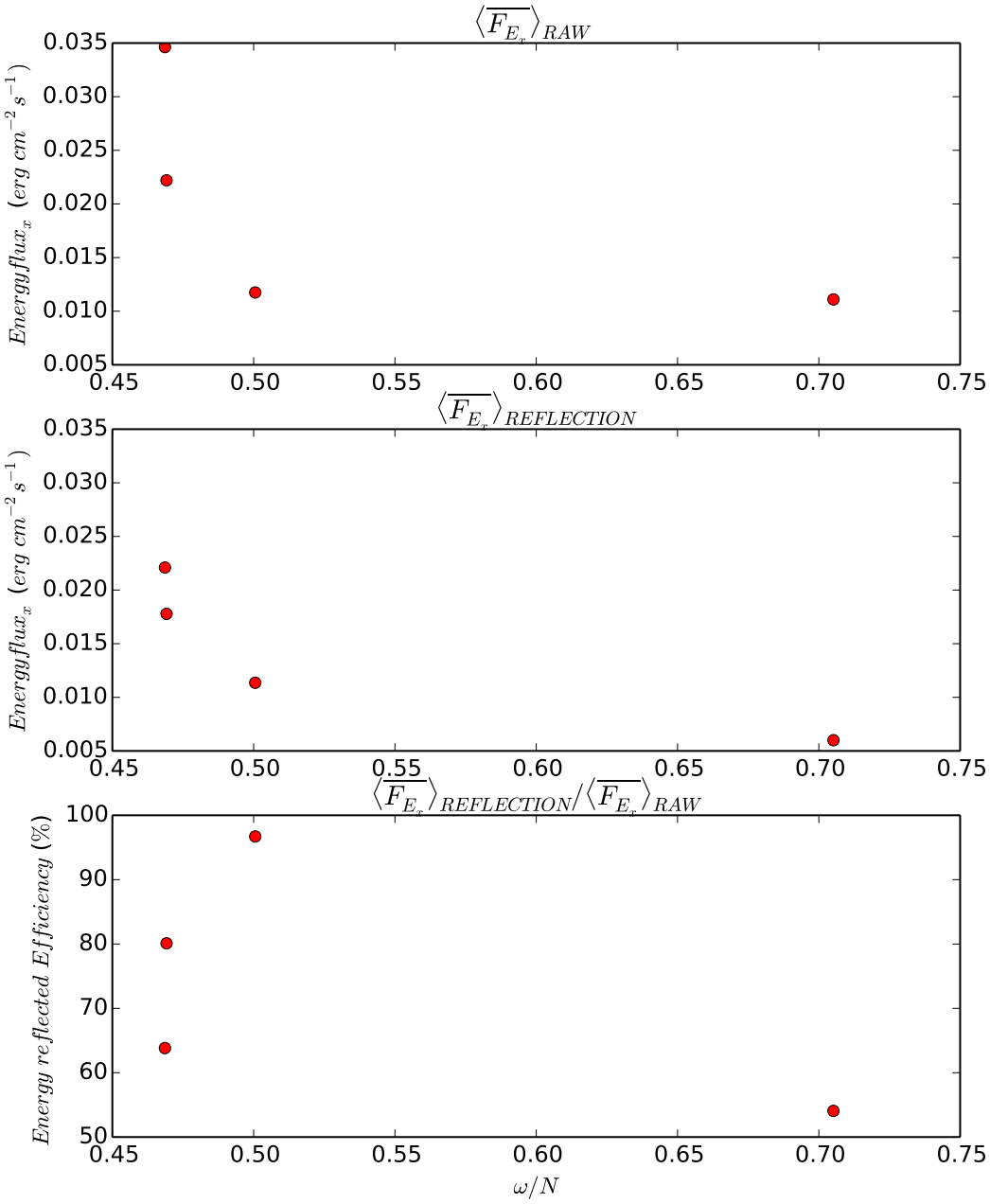

Figure 4.5: fig shows for case 2: super-critical slope, a) $\langle \overline{F_{E_x}} \rangle$ field of raw internal waves, b) $\langle \overline{F_{E_x}} \rangle$ field of reflected internal waves and c) the ratio $\langle \overline{F_{E_x}} \rangle$ field of reflected internal waves/ $\langle \overline{F_{E_x}} \rangle$ field of raw internal waves

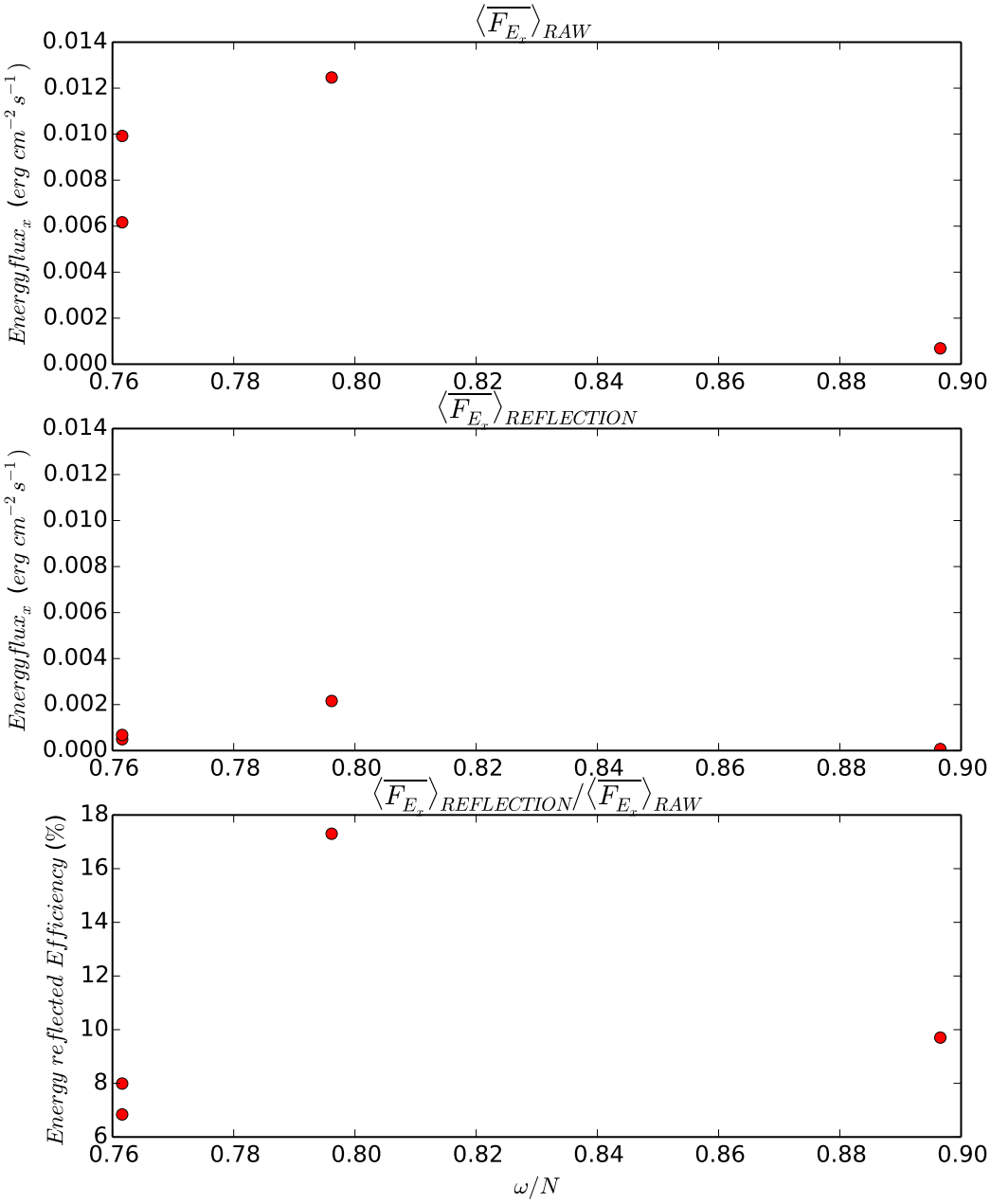

Figure 4.6: Figure shows for case 3: sub-critical slope a) $\langle\overline{F_{E_x}}\rangle$ field of raw internal waves, b) $\langle\overline{F_{E_x}}\rangle$ field of reflected internal waves and c) The ratio $\langle\overline{F_{E_x}}\rangle$ field of reflected internal waves/ $\langle\overline{F_{E_x}}\rangle$ field of raw internal waves

In the vertical time series of case 2 experiments we saw what appeared to be reflecting mode-2 internal waves. We need to realize additional experiments and do fourier analysis on the vertical time series of the reflected waves in case 2 experiments to know more.

Bibliography

[1] SB Dalziel, GO Hughes, and BR Sutherland. Whole-field density measurements by 'synthetic schlieren'. *Experiments in Fluids*, 28(4):322–335, 2000.

[2] C Garrett and E Kunze. Internal tide generation in the deep ocean. *Annual Review of Fluid Mechanics*, 39(1):57–87, 2007.

[3] L. Gostiaux, H. Didelle, S. Mercier, and T. Dauxois. A novel internal waves generator. *Experiments in Fluids*, 42(1):123–130, 2007.

[4] P Hyder, DRG Jeans, E Cauquil, and R Nerzic. Observations and predictability of internal solitons in the northern andaman sea. *Applied Ocean Research*, 27(1):1–11, 2005.

[5] Matthieu J Mercier, Nicolas B Garnier, and T Dauxois. Reflection and diffraction of internal waves analyzed with the hilbert transform. *Physics of Fluids (1994-present)*, 20(8):086601, 2008.

[6] MJ Mercier, Denis Martinand, M Mathur, L. Gostiaux, T Peacock, and T Dauxois. New wave generation. *Journal of Fluid Mechanics*, 657:308–334, 2010.

[7] DE Mowbray and BSH Rarity. The internal wave pattern produced by a sphere moving vertically in a density stratified liquid. *Journal of Fluid Mechanics*, 30(03):489–495, 1967.

[8] DE Mowbray and BSH Rarity. A theoretical and experimental investigation of the phase configuration of internal waves of small amplitude in a density stratified liquid. *Journal of Fluid Mechanics*, 28(01):1–16, 1967.

[9] P Mtfller. On the diffusion of momentum and mass by internal gravity waves. *Journal of Fluid Mechanics*, 77:789–823, 10 1976.

[10] Walter H Munk. Abyssal recipes. In *Deep Sea Research and Oceanographic Abstracts*, volume 13, pages 707–730. Elsevier, 1966.

[11] AR Osborne, TL Burch, RI Scarlet, et al. The influence of internal waves on deep-water drilling. *Journal of Petroleum Technology*, 30(10):1–497, 1978.

[12] J Sharples, C Mark Moore, Anna E Hickman, Patrick M Holligan, Jacqueline F Tweddle, Matthew R Palmer, and John H Simpson. Internal tidal mixing as a control on continental margin ecosystems. *Geophysical Research Letters*, 36(23), 2009.

[13] BR Sutherland. *Internal gravity waves*. Cambridge University Press, 2010.

[14] BR Sutherland, SB Dalziel, Graham O Hughes, and PF Linden. Visualization and measurement of internal waves by 'synthetic schlieren'. part 1. vertically oscillating cylinder. *Journal of fluid mechanics*, 390:93–126, 1999.

[15] A Toepler. *Beobachtungen nach einer neuen optischen Methode, etc.* 1864.

[16] Wikipedia. Snell's law — wikipedia, the free encyclopedia, 2014. [Online; accessed 14-June-2014].